The effect of the zero-field splitting interaction in light-induced pulsed dipolar EPR spectroscopy

Andreas Scherer, Berk Yildirim, Malte Drescher

5 Department of Chemistry and Konstanz Research School Chemical Biology, University of Konstanz, 78457 Konstanz, Germany

Correspondence to: Malte Drescher (malte.drescher@uni-konstanz.de)

Abstract. Laser-induced magnetic dipole spectroscopy (LaserIMD) and light-induced double electron-electron resonance spectroscopy (LiDEER) are important techniques in the emerging field of light-induced pulsed dipolar EPR spectroscopy

10 (light-induced PDS). These techniques use the photoexcitation of a chromophore to the triplet state and measure its dipolar coupling to a neighboring electron spin, which allows the determination of distance restraints. LaserIMD and LiDEER were so far analyzed with software tools that were developed for a pair of two $S = 1/2$ spins and neglect the zero-field splitting interaction (ZFS) of the excited triplet. Here, we show that the ZFS cannot be neglected in light-induced PDS, as it has an effect on the shape of the dipolar trace. For a detailed understanding of the effect of the ZFS, a theoretical description for

15 LaserIMD and LiDEER is derived, taking into account the non-secular terms of the ZFS. Simulations based on this model show that the ZFS leads to an additional decay in the dipolar trace in LaserIMD. This effect is not so pronounced in Q-band but can be quite noticeable for lower magnetic fields like in X-band. Experimentally recorded LiDEER and LaserIMD data confirm these findings and show that the ZFS is an important parameter that needs to be considered for the accurate description of light-induced PDS.

20 **1 Introduction**

Pulsed dipolar EPR spectroscopy (PDS) has become an important tool for nanoscale distance determination in soft matter. Its applications include the structural determination of biomacromolecules like proteins (Yee et al., 2015; Yang et al., 2020; Giannoulis et al., 2020; Weickert et al., 2020; Robotta et al., 2014; Ritsch et al., 2022), DNA (Wojciechowski et al., 2015; Takeda et al., 2004; Marko et al., 2011) and RNA (Collauto et al., 2020), but also synthetic polymers (Jeschke et al., 2010) as

25 well as nanoparticles (Hintze et al., 2015; Bücker et al., 2019). PDS measures the dipolar coupling between two spin centers within the molecule under investigation. Oftentimes, the spin centers need to be introduced as spin labels via site-directed labeling, with nitroxide spin probes as the most common example (Hubbell et al., 2013; Roser et al., 2016; García-Rubio, 2020). The most common PDS technique is double electron-electron resonance spectroscopy (DEER, also called PELDOR) (Jeschke, 2012). Here, one of the spin labels is excited by microwave pulses at an observer frequency to generate a refocused echo. The excitation of the other spin label by a pump pulse at a second frequency leads to an oscillation of the refocused echo,

when the pump pulse is shifted in the time domain. The frequency of this oscillation depends on the inverse cubic distance between the spin labels r^{-3} and thus provides distance information for the molecule under investigation (Jeschke, 2012).

The recent years have seen an advent of a new type of spin label, which are in an EPR-silent singlet ground state, but can be converted transiently to a triplet state by photoexcitation and subsequent inter-system crossing (Bertran et al., 2022). By now,

5 several of these transient triplet labels like porphyrins (Dal Farra et al., 2019b), fullerenes (Krumkacheva et al., 2019; Timofeev et al., 2022), Rose Bengal, Eosin Y and Atto Thio12 (Serrer et al., 2019; Williams et al., 2020) have been used. The most common PDS techniques for transient triplet labels are light-induced DEER (LiDEER) and laser-induced magnetic dipole spectroscopy (LaserIMD) (Di Valentin et al., 2014; Hintze et al., 2016). They both allow the determination of distances between one permanent spin label and one transient triplet label. LiDEER is a modification of DEER with an additional laser

10 flash preceding the microwave pulses. The transient triplet label is observed and the permanent spin is excited by the pump pulse (Figure 1a). In LaserIMD, on the other side, the permanent spin label is observed. During the evolution of the observer spin, the transient triplet label is excited by a laser flash (Figure 1b). The induced transition from the singlet to the triplet state has the equivalent effect as the microwave pump pulse in DEER and results in an oscillation of the echo of the observer spin. An advantage of LaserIMD is that, in contrast to DEER, the bandwidth of the laser excitation is neither limited by the width

15 of the EPR spectrum of the pump spin nor the resonator bandwidth. This gives a virtually infinite excitation bandwidths and promises high modulation depths also in cases where the microwave excitation bandwidth is smaller than the EPR spectra of the invoked spins (Scherer et al., 2022).

a) LiDEER
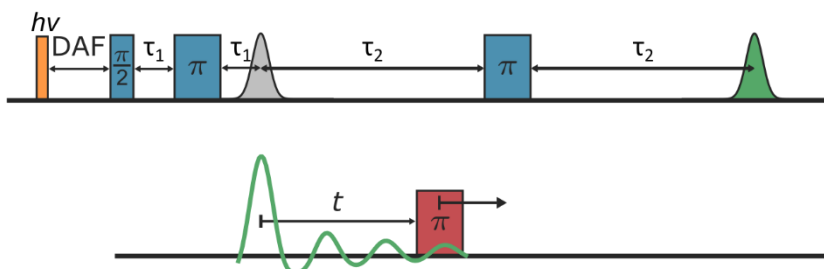
b) LaserIMD
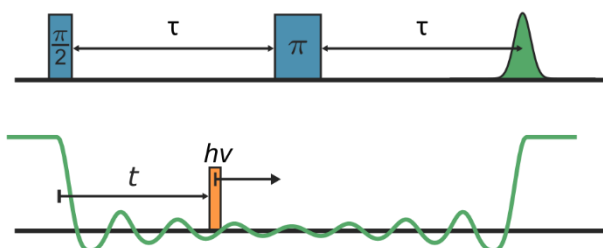
Figure 1: The pulse sequences of a) LiDEER and b) LaserIMD. The observed green echoes are modulated when the pump pulse (LiDEER) or laser flash (LaserIMD) is shifted in the time domain.

In previous works, LaserIMD and LiDEER data were analyzed under the assumption that contributions from the zero-field splitting interaction (ZFS) can be ignored (Di Valentin et al., 2014; Hintze et al., 2016; Bieber et al., 2018; Dal Farra et al., 2019a; Krumkacheva et al., 2019), which means that the dipolar traces have the same shape as those for a $S = 1/2$ spin pair. This is correct if all spin-spin interactions are much smaller than the Zeeman-interaction with the external magnetic field.

5 Then, all non-secular terms in the Hamiltonian can be dropped (Manukovsky et al., 2017). Most PDS experiments like e.g. nitroxide-nitroxide DEER can be analyzed with this assumption (Jeschke et al., 2006; Fábregas Ibáñez et al., 2020). The excited triplet state of transient triplet labels with a total spin of $S = 1$, however, can be subject to a strong ZFS, reaching values over 1 GHz in many cases (Di Valentin et al., 2014; Williams et al., 2020). For other high-spin labels like Gd[III] or high-spin Fe[III], it is already known that the ZFS can have an effect on the recorded dipolar trace and that it has to be included in the data-

10 analysis routine, if artefacts in the distance shall be avoided (Dalaloyan et al., 2015; Abdullin et al., 2019).

Here, we set out to investigate the effect of the ZFS in light-induced PDS. Therefore, we are going to derive a theoretical description for light-induced PDS taking the $S = 1$ spin state and ZFS of the triplet state into account. Section 3 will report about the materials and methods used. In section 4, the theoretical model will be used for numerical simulations of LaserIMD and time-domain simulations were performed for LiDEER. It will be shown that in both methods, but particularly in LaserIMD,

15 the effect of the ZFS can result in significant differences in the dipolar traces compared to the $S = 1/2$ case where the ZFS is ignored. In section 5, experimental LaserIMD and LiDEER traces are shown and the influence of the ZFS is discussed by comparing the model with the experimental data.

2 Theoretical derivation

2.1 DEER

20 In DEER, one typically uses the assumption that both spins are of $S = 1/2$ nature and the system is in high-field and weak-coupling limit so that all pseudo- and non-secular parts of the spin Hamiltonian can be dropped (Fábregas Ibáñez et al., 2020). In this case, there are two coherence transfer pathways that contribute to the DEER signal; one where the pump spin is flipped from the state with $m_S = +1/2$ to $m_S = -1/2$, and the one where it is flipped from $m_S = -1/2$ to $m_S = +1/2$. The frequency of the dipolar oscillation of the refocused echo for the two coherence transfer pathways is (Sweger et al., 2022):

$$\omega_{\text{DEER}, +\frac{1}{2} \to -\frac{1}{2}} = \left(3\cos(\beta_{\text{dip}})^2 - 1\right)\omega_{\text{dip}}. \tag{1}$$

$$\omega_{\text{DEER}, -\frac{1}{2} \to +\frac{1}{2}} = -\left(3\cos(\beta_{\text{dip}})^2 - 1\right)\omega_{\text{dip}}. \tag{2}$$

25 Here, β_{dip} is the angle between the dipolar coupling vector and the external magnetic field and ω_{dip} is the dipolar coupling in radial frequency units. It depends on the distance r between the two labels (Pannier et al., 2000; Schweiger and Jeschke, 2001; Jeschke, 2012):

$$\omega_{\text{dip}} = \frac{\mu_B^2 g_1 g_2}{\hbar} \frac{1}{r^3}, \tag{3}$$

With the Bohr-magneton μ_B, the reduced Plank constant $\hbar$, and the g-values g_1 and g_2 of the two spin labels. In experiments one typically measures powder samples, thus molecules with all orientations with respect to the external field contribute to the signal, and the weighted integral over all angles β_{dip} must be taken (Edwards and Stoll, 2018). In the high-temperature limit, which is often fulfilled in experiments, the population of the spin states with $m_S = +1/2$ to $m_S = -1/2$ is virtually identical and therefore both coherence transfer pathways contribute equally to the signal (Marko et al., 2013). In this case the integral over all orientations is:

$$S_{\text{DEER}}(t,r) = \int_0^{\pi/2} d\beta_{\text{dip}} \sin(\beta_{\text{dip}}) \cos\left(t\left(3\cos(\beta_{\text{dip}})^2 - 1\right)\omega_{\text{dip}}(r)\right) \tag{4}$$

Here, t is the time at which the pump pulse flips the pump spins. Due to a limited excitation bandwidth and pulse imperfections not all spins can be excited by the pump pulse, therefore a part of the signal is not modulated:

$$F_{\text{DEER}}(t,r) = \lambda S_{\text{DEER}}(t,r) + (1 - \lambda), \tag{5}$$

where the modulation depth λ depends on the fraction of excited pump spins. The experimental signal is the product of this intramolecular contribution $F_{\text{DEER}}(t,r)$ and a contribution from the intermolecular dipolar interactions $B(t)$, that is typically termed background (Jeschke, 2016). Finally, the contributions from all distances need to be included by integrating over the distance distribution $P(r)$:

$$V_{\text{DEER}}(t) = \int dr K_{\text{DEER}}(t,r)P(r) = \int dr B(t)F_{\text{DEER}}(t,r)P(r). \tag{6}$$

The kernel $K_{\text{DEER}}(t,r)$ describes the relation between the distance distribution and the measured dipolar trace in DEER. In a sample with a homogenous distribution of spins, the background function can be obtained by integrating over all dipolar interactions within the sample, which results in (Hu and Hartmann, 1974):

$$B(t) = \exp(-k|t|). \tag{7}$$

The decay constant k is proportional to the spin concentration and modulation depth (Hu and Hartmann, 1974). By inverting Eq. (6), it is possible to extract the distance distribution $P(r)$ from the experimentally recorded signal $V_{\text{DEER}}(t)$. Because this is an ill-posed problem, this is typically done by advanced techniques like Tikhonov regularization or neural networks (Edwards and Stoll, 2018; Worswick et al., 2018).

2.2 LaserIMD

In LaserIMD, the spin system consists of a permanent spin label, which serves as an observer spin, and a transient triplet label, which is excited by a laser flash. In many cases, the permanent spin label is or can be assumed to be a doublet with $S_D = 1/2$. Before the photoexcitation, the transient label is still in its singlet state and does therefore neither interact with the external field B, nor with the doublet S_D. The Hamiltonian thus only contains the Zeeman interaction of S_D:

$$\hat{H}_{\text{dark}} = \omega_{\text{D}} \hat{S}_{\text{D},z}, \tag{8}$$

with the Zeeman frequency $\omega_{\text{D}} = \frac{g_{\text{D}}\mu_{\text{B}}}{\hbar} B$, g_{D} the g-values of S_{D}, which is assumed to be isotropic. The Hamiltonian is written in units of radial frequencies. This Hamiltonian has two eigenvalues:

$$E_{+\frac{1}{2}, \text{dark}} = \frac{\omega_{\text{D}}}{2}, \tag{9}$$

$$E_{-\frac{1}{2}, \text{dark}} = -\frac{\omega_{\text{D}}}{2}. \tag{10}$$

When the laser flash excites the transient triplet label to the triplet state $S_{\text{T}} = 1$, the Zeeman interaction of S_{T}, the ZFS between the two unpaired electrons that form the triplet S_{T} and the dipolar coupling between S_{D} and S_{T} has to be included in the

5 Hamiltonian:

$$\hat{H} = \omega_{\text{D}} \hat{S}_{\text{D},z} + \omega_{\text{T}} \hat{S}_{\text{T},z} + \boldsymbol{S}_{\text{T}} \cdot \mathbf{D} \cdot \boldsymbol{S}_{\text{T}} + \boldsymbol{S}_{\text{T}} \cdot \mathbf{T} \cdot \boldsymbol{S}_{\text{D}}. \tag{11}$$

Here, $\omega_{\text{T}} = \frac{g_{\text{T}}\mu_{\text{B}}B}{\hbar}$ is the Zeeman frequency of the spin S_{T} with its isotropic g-value g_{T}. $\bar{S}_{\text{D}}$ and $\bar{S}_{\text{T}}$ represent the vectors of the Cartesian spin operators $\boldsymbol{S}_{\text{D}} = \left(\hat{S}_{\text{D},x}, \hat{S}_{\text{D},y}, \hat{S}_{\text{D},z}\right)^{\text{T}}$ and $\boldsymbol{S}_{\text{T}} = \left(\hat{S}_{\text{T},x}, \hat{S}_{\text{T},y}, \hat{S}_{\text{T},z}\right)^{\text{T}}$. The ZFS tensor $\mathbf{D}$ is described by the ZFS values $D = \frac{3}{2}D_z$ and $E = \frac{D_x - D_y}{2}$, where D_x, D_y and D_z are the eigenvalues of the ZFS tensor (Telser, 2017). Its orientation is described by the three Euler angles α_T, β_T and γ_T that connect the laboratory frame with the molecular frame of the transient triplet label.

10 The dipolar coupling tensor $\mathbf{T}$ is axial with its eigenvalues being $T_x = T_y = -\omega_{\text{dip}}$ and $T_z = 2\omega_{\text{dip}}$ (Schweiger and Jeschke, 2001). Its orientation towards the external magnetic field is described by the angle β_{dip}.

In the literature up to now, a high-field and weak-coupling limit is typically assumed for LaserIMD, so that all non- and pseudo-secular terms were dropped from the Hamiltonian (Hintze et al., 2016; Dal Farra et al., 2019b). The remaining secular Hamiltonian (see Eq. (S2) in S1) is already diagonal in the high-field basis with the energy levels $E^{\text{sec}}_{m_{\text{D}}, m_{\text{T}}}$, where m_{D} and m_{T}

15 are the magnetic quantum numbers of the doublet S_{D} and the triplet S_{T}. The exact expressions for the energies $E^{\text{sec}}_{m_{\text{D}}, m_{\text{T}}}$ can be found in Eq. (S4) -(S9) in S1. In LaserIMD, the initial $\frac{\pi}{2}$-pulse generates a coherence of the observer spin S_{D}. Before the laser excitation, the coherence evolves with a frequency of $E_{+\frac{1}{2}, \text{dark}} - E_{-\frac{1}{2}, \text{dark}} = \omega_{\text{D}}$, it is not influenced by the dipolar coupling because the transient triplet label is still in a singlet state with $S_{\text{T}} = 0$ and $m_{\text{T}} = 0$. The excitation of the transient triplet label leads to three different coherence transfer pathways, depending to which manifold $m_{\text{T}} = 1, 0$ or -1 of the triplet the transient

20 label is excited to. Depending on the triplet state m_T, the coherence will then continue to evolve with $E^{\text{sec}}_{+\frac{1}{2}, m_{\text{T}}} - E^{\text{sec}}_{-\frac{1}{2}, m_{\text{T}}}$. The refocusing π-pulse generates an echo at the time 2τ. Due to the different frequencies before and after the excitation at a variable time t, the coherences are not completely refocused but depending on the time of the laser flash they will have gained a phase $\phi = \omega^{\text{sec}}_{m_{\text{T}}} t$, that depends on the LaserIMD frequency $\omega^{\text{sec}}_{m_{\text{T}}}$ of the corresponding triplet manifold m_{T}. When only the secular terms are considered in the Hamiltonian, the LaserIMD frequencies $\omega^{\text{sec}}_{m_{\text{T}}}$ do not dependent on the ZFS, because its secular

25 terms cancel each other out (Hintze et al., 2016):

$$\omega_{+1}^{\text{sec}} = \left(E_{+\frac{1}{2}, +1}^{\text{sec}} - E_{-\frac{1}{2}, +1}^{\text{sec}}\right) - \left(E_{+\frac{1}{2}, \text{dark}} - E_{-\frac{1}{2}, \text{dark}}\right) = \left(3\cos(\beta_{\text{dip}})^2 - 1\right)\omega_{\text{dip}}, \tag{12}$$

$$\omega_0^{\text{sec}} = \left(E_{+\frac{1}{2}, 0}^{\text{sec}} - E_{-\frac{1}{2}, 0}^{\text{sec}}\right) - \left(E_{+\frac{1}{2}, \text{dark}} - E_{-\frac{1}{2}, \text{dark}}\right) = 0, \tag{13}$$

$$\omega_{-1}^{\text{sec}} = \left(E_{+\frac{1}{2}, -1}^{\text{sec}} - E_{-\frac{1}{2}, -1}^{\text{sec}}\right) - \left(E_{+\frac{1}{2}, \text{dark}} - E_{-\frac{1}{2}, \text{dark}}\right) = -\left(3\cos(\beta_{\text{dip}})^2 - 1\right)\omega_{\text{dip}}. \tag{14}$$

When the transient triplet label is excited to $m_{\text{T}} = 1$ or $m_{\text{T}} = -1$, the LaserIMD frequencies in secular-approximation from Eq. (12) and (14) are identical to the DEER frequencies in Eq. (1) and (2). Here, the laser flash leads to a change in the magnetic quantum number of $\Delta m_{\text{T}} = \pm 1$, which is equivalent to the effect of the microwave pump pulse in DEER. In the case when the transient triplet label is excited to the state $m_{\text{T}} = 0$, however, the secular approximation predicts that the echo is not oscillating,

5 because -loosely spoken- there is no change in the magnetic spin quantum number of the transient triplet label, which means that the dipolar coupling is not changed. Like it is the case in DEER, the measured signal is the average over all orientations of the spin system. Whereas in DEER it is only necessary to consider the orientation of the dipolar vector, in LaserIMD the orientation of the transient triplet label must also be taken into account, therefore it is necessary to also integrate over the three corresponding Euler angles α_{T}, β_T and γ_{T} (Bak and Nielsen, 1997). As the triplet state of the transient label is reached by

10 intersystem-crossing, the population of the three high-field triplet states $m_{\text{T}} = +1, 0, -1$ depends on the orientation of the transient label with respect to the external magnetic field and the populations P_x, P_y and P_z of the zero-field eigenstates of the ZFS (Williams et al., 2020; McLauchlan et al., 1994). The contribution of the three coherence transfer pathways must be weighted by population of these high-field states; this gives (still in secular approximation) the three expressions:

$$S_{+1}^{\text{sec}}(t,r) = \frac{1}{8\pi^2}\int_0^{2\pi} d\alpha_{\text{T}} \int_0^\pi d\beta_{\text{T}} \sin(\beta_{\text{T}}) \int_0^{2\pi} d\gamma_{\text{T}} \left(\frac{P_z}{2}\sin^2(\beta_{\text{T}}) + \frac{P_x}{2}\left(\cos^2(\beta_{\text{T}}) + \sin^2(\beta_{\text{T}})\sin^2(\gamma_{\text{T}})\right)\right.$$
$$\left. + \frac{P_y}{2}\left(\cos^2(\beta_{\text{T}}) + \sin^2(\beta_{\text{T}})\cos^2(\gamma_{\text{T}})\right)\right)\int_0^{\frac{\pi}{2}} d\beta_{\text{dip}} \sin(\beta_{\text{dip}}) \exp\left(-i\omega_{+1}^{\text{sec}}(\beta_{\text{dip}})t\right), \tag{15}$$

$$S_0^{\text{sec}}(t,r) = \frac{1}{8\pi^2}\int_0^{2\pi} d\alpha_{\text{T}} \int_0^\pi d\beta_{\text{T}} \sin(\beta_{\text{T}}) \int_0^{2\pi} d\gamma_{\text{T}}\left(P_z\cos^2(\beta_{\text{T}}) + P_x\sin^2(\beta_{\text{T}})\cos^2(\gamma_{\text{T}})\right.$$
$$\left. + P_y\sin^2(\beta_{\text{T}})\sin^2(\gamma_{\text{T}})\right)\int_0^{\pi/2} d\beta_{\text{dip}} \sin(\beta_{\text{dip}}) \exp\left(-i\omega_0^{\text{sec}}(\beta_{\text{dip}})t\right), \tag{16}$$

$$S_{-1}^{\text{sec}}(t,r) = \frac{1}{8\pi^2}\int_0^{2\pi} d\alpha_{\text{T}} \int_0^\pi d\beta_{\text{T}} \sin(\beta_{\text{T}}) \int_0^{2\pi} d\gamma_{\text{T}} \left(\frac{P_z}{2}\sin^2(\beta_{\text{T}}) + \frac{P_x}{2}\left(\cos^2(\beta_{\text{T}}) + \sin^2(\beta_{\text{T}})\sin^2(\gamma_{\text{T}})\right)\right.$$
$$\left. + \frac{P_y}{2}\left(\cos^2(\beta_{\text{T}}) + \sin^2(\beta_{\text{T}})\cos^2(\gamma_{\text{T}})\right)\right)\int_0^{\frac{\pi}{2}} d\beta_{\text{dip}} \sin(\beta_{\text{dip}}) \exp\left(-i\omega_{-1}^{\text{sec}}(\beta_{\text{dip}})t\right). \tag{17}$$

Performing the integration over the orientations of the transient label α_T, β_T and γ_T and taking the sum gives (Williams et al., 2020):

$$S_\mathrm{LaserIMD}^\mathrm{sec}(t,r) = S_{+1}^\mathrm{sec}(t,r) + S_0^\mathrm{sec}(t,r) + S_{-1}^\mathrm{sec}(t,r) = \frac{2}{3}\int_0^{\pi/2}\cos\big(\omega_\mathrm{dip}(3\cos^2(\beta_\mathrm{dip}) - 1)t\big)\sin(\beta_\mathrm{dip})\,\mathrm{d}\beta_\mathrm{dip} + \frac{1}{3}$$

$$= \frac{2}{3}\,S_\mathrm{DEER}(t,r) + \frac{1}{3}. \tag{18}$$

In secular-approximation, the first term of the LaserIMD signal is equivalent to the trace $S_\mathrm{DEER}^\mathrm{sec}(t)$ (Edwards and Stoll, 2018). The second term, however, is a non-modulated contribution. For the final expression for the kernel $K_\mathrm{LaserIMD}^\mathrm{sec}(t,r)$, the quantum yield of the triplet state is considered by an additional factor γ and the intermolecular interaction to other spins in the sample has to be considered as background $B(t)$:

$$K_\mathrm{LaserIMD}^\mathrm{sec}(t,r) = B(t)(\gamma S_\mathrm{LaserIMD}^\mathrm{sec}(t,r) + 1 - \gamma). \tag{19}$$

This can be rewritten as:

$$K_\mathrm{LaserIMD}^\mathrm{sec}(t,r) = B(t)(\lambda S_\mathrm{DEER}(t,r) + 1 - \lambda), \tag{20}$$

with the modulation depth $\lambda = 2/3\gamma$. The only difference between LaserIMD in the secular approximation and DEER is that in LaserIMD, even for a triplet yield of $\gamma = 100\,\%$, there is coherence transfer pathway with $\Delta m_S = 0$ that does not result in a dipolar oscillation, which limits the maximum achievable modulation depth to $66.\bar{6}\,\%$. If the secular approximation can be employed in LaserIMD, this means that it is possible to analyze experimentally recorded LaserIMD data with the same kernel that can be used for DEER and no new analysis routine needs to be implemented.

Even though in the secular approximation the ZFS has no effect in LaserIMD, it cannot be taken for granted that the non-secular terms can be ignored because the ZFS of some transient triplet labels can be quite large (Williams et al., 2020). In Figure 2 it is shown, how the energy levels $E_{m_\mathrm{D},m_\mathrm{T}}^\mathrm{non-sec}$ get shifted when additional non-secular terms of the ZFS and dipolar coupling are considered. This shift was calculated by including the non-secular terms from Eq. (S3) in S1 and diagonalizing the Hamiltonian with a second-order perturbation approach (Hagston and Holmes, 1980). This is described in detail in S1. Please note that we did not consider all non-secular terms and pseudo-secular terms were also ignored. It is shown in S2 that at magnetic field strengths that are relevant for experimental conditions the included non-secular terms from Eq. (S3) are sufficient and no further distortions are to be expected by the left-out ones.
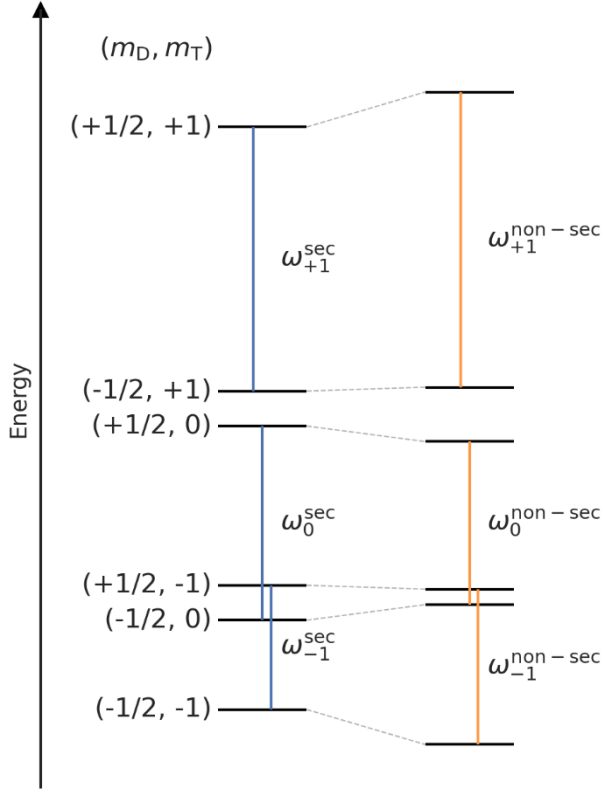
Figure 2: Energy level diagram (not to scale) after the transient triplet label has been excited to the triplet state demonstrating the shift that is induced by the non-secular terms of the ZFS and dipolar coupling from Eq. (S3). The energy levels in secular approximation are shown on the left and the levels with the non-secular terms are shown on the right. The vertical lines in blue (secular approximation) and orange (non-secular terms included) indicate the coherences of the permanent spin label that are excited during the LaserIMD pulse sequence. They are marked with the corresponding transition frequencies.

The shift of the energy levels also leads to a shift in the LaserIMD frequencies.

$$\omega_{+1}^{\text{non-sec}} = \left(E_{+\frac{1}{2}, +1}^{\text{non-sec}} - E_{-\frac{1}{2}, +1}^{\text{non-sec}} \right) - \left(E_{+\frac{1}{2}, \text{dark}} - E_{-\frac{1}{2}, \text{dark}} \right) = \left(\left(3\cos\left(\beta_{\text{dip}}\right)^2 - 1 \right) + \delta_{\text{ZFS}}\sin\left(2\beta_{\text{dip}}\right) \right) \omega_{\text{dip}}, \tag{21}$$

$$\omega_{0}^{\text{non-sec}} = \left(E_{+\frac{1}{2}, 0}^{\text{non-sec}} - E_{-\frac{1}{2}, 0}^{\text{non-sec}} \right) - \left(E_{+\frac{1}{2}, \text{dark}} - E_{-\frac{1}{2}, \text{dark}} \right) = -2\delta_{\text{ZFS}}\sin\left(2\beta_{\text{dip}}\right) \omega_{\text{dip}}, \tag{22}$$

$$\omega_{-1}^{\text{non-sec}} = \left(E_{+\frac{1}{2}, -1}^{\text{non-sec}} - E_{-\frac{1}{2}, -1}^{\text{non-sec}} \right) - \left(E_{+\frac{1}{2}, \text{dark}} - E_{-\frac{1}{2}, \text{dark}} \right) = \left(-\left(3\cos\left(\beta_{\text{dip}}\right)^2 - 1 \right) + \delta_{\text{ZFS}}\sin\left(2\beta_{\text{dip}}\right) \right) \omega_{\text{dip}}, \tag{23}$$

with

$$\delta_{\text{ZFS}} = \frac{3\sin(2\beta_{\text{T}})\cos(\alpha_{\text{T}})D - 6\sin(\beta_{\text{T}})(\cos(\beta_{\text{T}})\cos(2\gamma_{\text{T}})\cos(\alpha_{\text{T}}) - \sin(2\gamma_{\text{T}})\sin(\alpha_{\text{T}}))E}{4\omega_{\text{T}}}. \tag{24}$$

As can be seen from Eq. (21) -(23), the frequencies $\omega_{+1}^{\text{non-sec}}$ and $\omega_{-1}^{\text{non-sec}}$ are the sum of the unperturbed frequencies ω_{+1}^{sec} and ω_{-1}^{sec} and a frequency shift $\delta_{\text{ZFS}}\sin(2\beta_{\text{dip}})\omega_{\text{dip}}$, which contains the effect of the ZFS. Most notably, the coherence transfer pathway with $\Delta m_{\text{T}} = 0$ does not lead to a vanishing LaserIMD frequency as it was the case in the secular approximation.

5 Instead, we find that $\omega_0^{\text{non-sec}}$ equals twice the negative of the frequency shift that is experienced by the other two coherence transfer pathways. The frequency shift scales with δ_{ZFS} that depends on the ZFS values D and E, the Zeeman frequency of the transient triplet label ω_{T} as well as the orientation of the transient triplet label, described by α_{T}, β_{T} and γ_{T}. At a higher ZFS and a smaller magnetic field, the shift of the LaserIMD frequencies will be larger, so that larger disturbances in the LaserIMD trace can be expected in these cases.

10 The integrals for the powder are more complex when the non-secular terms are included, because the LaserIMD frequencies now also depend on the orientation of the transient triplet label:

$$S_{+1}^{\text{non-sec}}(t,r) = \frac{1}{8\pi^2}\int_0^{2\pi}\mathrm{d}\alpha_t\int_0^{\pi}\mathrm{d}\beta_t\sin(\beta_t)\int_0^{2\pi}\mathrm{d}\gamma_t\left(\frac{P_z}{2}\sin^2(\beta_t) + \frac{P_x}{2}(\cos^2(\beta_t) + \sin^2(\beta_t)\sin^2(\gamma_t))\right.$$
$$\left. + \frac{P_y}{2}(\cos^2(\beta_t) + \sin^2(\beta_t)\cos^2(\gamma_t))\right)\int_0^{\frac{\pi}{2}}\mathrm{d}\beta_{\text{dip}}\sin(\beta_{\text{dip}})\exp(-i\omega_{+1}^{\text{non-sec}}(\alpha_{\text{T}},\beta_{\text{T}},\gamma_{\text{T}},\beta_{\text{dip}})t), \tag{25}$$

$$S_0^{\text{non-sec}}(t,r) = \frac{1}{8\pi^2}\int_0^{2\pi}\mathrm{d}\alpha_{\text{T}}\int_0^{\pi}\mathrm{d}\beta_{\text{T}}\sin(\beta_{\text{T}})\int_0^{2\pi}\mathrm{d}\gamma_{\text{T}}\left(P_z\cos^2(\beta_{\text{T}}) + P_x\sin^2(\beta_{\text{T}})\cos^2(\gamma_{\text{T}})\right.$$
$$\left. + P_y\sin^2(\beta_{\text{T}})\sin^2(\gamma_{\text{T}})\right)\int_0^{\pi/2}\mathrm{d}\beta_{\text{dip}}\sin(\beta_{\text{dip}})\exp(-i\omega_0^{\text{non-sec}}(\alpha_{\text{T}},\beta_{\text{T}},\gamma_{\text{T}},\beta_{\text{dip}})t), \tag{26}$$

$$S_{-1}^{\text{non-sec}}(t,r) = \frac{1}{8\pi^2}\int_0^{2\pi}\mathrm{d}\alpha_{\text{T}}\int_0^{\pi}\mathrm{d}\beta_{\text{T}}\sin(\beta_t)\int_0^{2\pi}\mathrm{d}\gamma_{\text{T}}\left(\frac{P_z}{2}\sin^2(\beta_{\text{T}}) + \frac{P_x}{2}(\cos^2(\beta_{\text{T}}) + \sin^2(\beta_{\text{T}})\sin^2(\gamma_{\text{T}}))\right.$$
$$\left. + \frac{P_y}{2}(\cos^2(\beta_{\text{T}}) + \sin^2(\beta_{\text{T}})\cos^2(\gamma_{\text{T}}))\right)\int_0^{\frac{\pi}{2}}\mathrm{d}\beta_{\text{dip}}\sin(\beta_{\text{dip}})\exp(-i\omega_{-1}^{\text{non-sec}}(\alpha_{\text{T}},\beta_{\text{T}},\gamma_{\text{T}},\beta_{\text{dip}})t). \tag{27}$$

The sum over these terms gives the final intramolecular contribution in LaserIMD.

$$S_{\text{LaserIMD}}^{\text{non-sec}}(t) = S_{+1}^{\text{non-sec}}(t) + S_0^{\text{non-sec}}(t) + S_{-1}^{\text{non-sec}}(t). \tag{28}$$

By including incomplete excitation and the intermolecular dipolar interactions, one arrives at the final model

$$K_{\text{LaserIMD}}^{\text{non-sec}}(t,r) = B(t)(\lambda S_{\text{LaserIMD}}^{\text{non-sec}}(t,r) + 1 - \lambda). \tag{29}$$

Unlike it was the case for the secular approximation, the integrals are difficult to solve analytically and further insight in these
15 expression will be gained by numerical integrations in the next sections. However, it can already be seen without further

calculations that with the non-secular terms the ZFS has an influence in LaserIMD and that the resulting kernel no longer corresponds to the kernel $K_{\text{DEER}}(t,r)$ of the $S = 1/2$ case.

2.3 LiDEER

In LiDEER, the transient triplet label is observed and the permanent spin label is pumped. For simplicity, we will derive the

5   expressions within the secular approximation first and afterwards turn to the case that includes the non-secular terms. Due to the limited excitation bandwidth of the observer pulse, either the transition between the states with $m_T = 1$ and $m_T = 0$ or the states with $m_T = 0$ and $m_T = -1$ of the transient triplet label is excited. If the transition between the states $m_T = 1$ and $m_T = 0$ is excited, the excited coherence of the triplet spin will either evolve with the frequency $\omega^{\text{sec}}_{+\frac{1}{2}, 1\leftrightarrow0} = E^{\text{sec}}_{+\frac{1}{2}, +1} - E^{\text{sec}}_{+\frac{1}{2}, 0}$ or $\omega^{\text{sec}}_{-\frac{1}{2}, 1\leftrightarrow0} = E^{\text{sec}}_{-\frac{1}{2}, +1} - E^{\text{sec}}_{-\frac{1}{2}, 0}$, depending on whether the permanent spin label is in the state with $m_D = 1/2$ or $m_D = -1/2$.

10   Pumping the permanent spin label at the time t will result in a transition from $m_D = +\frac{1}{2}$ to $m_D = -\frac{1}{2}$ -or vice versa- and the frequency $\omega^{\text{sec}}_{+\frac{1}{2}, 1\leftrightarrow0}$ or $\omega^{\text{sec}}_{-\frac{1}{2}, 1\leftrightarrow0}$ with which the coherence evolves will change accordingly. At the time of the echo, the coherence will have gained a phase $\phi = \omega^{\text{sec}}_{\pm\frac{1}{2}\rightarrow\mp\frac{1}{2}, +1\leftrightarrow0} t$, where $\omega^{\text{sec}}_{\pm\frac{1}{2}\rightarrow\mp\frac{1}{2}, +1\leftrightarrow0}$ are the LiDEER frequencies of the two coherence transfer pathways:

$$\omega^{\text{sec}}_{+\frac{1}{2}\rightarrow-\frac{1}{2}, +1\leftrightarrow0} = \left(E^{\text{sec}}_{+\frac{1}{2}, +1} - E^{\text{sec}}_{+\frac{1}{2}, 0}\right) - \left(E^{\text{sec}}_{-\frac{1}{2}, +1} - E^{\text{sec}}_{-\frac{1}{2}, 0}\right) = \left(3\cos(\beta_{\text{dip}})^2 - 1\right)\omega_{\text{dip}}, \tag{30}$$

$$\omega^{\text{sec}}_{-\frac{1}{2}\rightarrow+\frac{1}{2}, +1\leftrightarrow0} = \left(E^{\text{sec}}_{-\frac{1}{2}, +1} - E^{\text{sec}}_{-\frac{1}{2}, 0}\right) - \left(E^{\text{sec}}_{+\frac{1}{2}, 0} - E^{\text{sec}}_{+\frac{1}{2}, -1}\right) = -\left(3\cos(\beta_{\text{dip}})^2 - 1\right)\omega_{\text{dip}}. \tag{31}$$

When the other transition of the triplet spin from $m_T = 0$ and $m_T = -1$ is excited by the observer pulse, the frequencies are

15   the same:

$$\omega^{\text{sec}}_{+\frac{1}{2}\rightarrow-\frac{1}{2}, 0\leftrightarrow-1} = \left(E^{\text{sec}}_{+\frac{1}{2}, +1} - E^{\text{sec}}_{+\frac{1}{2}, 0}\right) - \left(E^{\text{sec}}_{-\frac{1}{2}, +1} - E^{\text{sec}}_{-\frac{1}{2}, 0}\right) = \left(3\cos(\beta_{\text{dip}})^2 - 1\right)\omega_{\text{dip}}, \tag{32}$$

$$\omega^{\text{sec}}_{-\frac{1}{2}\rightarrow+\frac{1}{2}, 0\leftrightarrow-1} = \left(E^{\text{sec}}_{-\frac{1}{2}, +1} - E^{\text{sec}}_{-\frac{1}{2}, 0}\right) - \left(E^{\text{sec}}_{+\frac{1}{2}, 0} - E^{\text{sec}}_{+\frac{1}{2}, -1}\right) = -\left(3\cos(\beta_{\text{dip}})^2 - 1\right)\omega_{\text{dip}}. \tag{33}$$

As those are the same frequencies as the ones in DEER with two $S = 1/2$ spins, one eventually arrives at the same kernel $K_{\text{DEER}}(t,r)$. This means that like it was the case in LaserIMD the secular terms of the ZFS cancel each other out, and there is no effect of the ZFS on the LiDEER trace. In contrast to LaserIMD in secular approximation, there are also no coherence transfer pathways with $\Delta m_D = 0$, so that the maximum achievable modulation depth in LiDEER is 100 %.

20   It seems obvious that the same non-secular terms that lead to change in the LaserIMD frequencies are also relevant in LiDEER. Therefore, the LiDEER frequencies were also determined from the energy levels $E^{\text{non-sec}}_{m_D, m_T}$ that include the effects of the ZFS:

$$\omega^{\mathrm{non-sec}}_{+\frac{1}{2}\to-\frac{1}{2},\,+1\leftrightarrow0} = \left(E^{\mathrm{non-sec}}_{+\frac{1}{2},\,+1} - E^{\mathrm{non-sec}}_{+\frac{1}{2},\,0}\right) - \left(E^{\mathrm{non-sec}}_{-\frac{1}{2},\,+1} - E^{\mathrm{non-sec}}_{-\frac{1}{2},\,0}\right)$$
$$= \left(\left(3\cos(\beta_{\mathrm{dip}})^2 - 1\right) + 3\delta_{\mathrm{ZFS}}\sin(2\beta_{\mathrm{dip}})\right)\omega_{\mathrm{dip}}, \tag{34}$$

$$\omega^{\mathrm{non-sec}}_{-\frac{1}{2}\to+\frac{1}{2},\,+1\leftrightarrow0} = \left(E^{\mathrm{non-sec}}_{-\frac{1}{2},\,+1} - E^{\mathrm{non-sec}}_{-\frac{1}{2},\,0}\right) - \left(E^{\mathrm{non-sec}}_{+\frac{1}{2},\,0} - E^{\mathrm{non-sec}}_{+\frac{1}{2},\,-1}\right)$$
$$= -\left(\left(3\cos(\beta_{\mathrm{dip}})^2 - 1\right) + 3\delta_{\mathrm{ZFS}}\sin(2\beta_{\mathrm{dip}})\right)\omega_{\mathrm{dip}}, \tag{35}$$

$$\omega^{\mathrm{non-sec}}_{+\frac{1}{2}\to-\frac{1}{2},\,0\leftrightarrow-1} = \left(E^{\mathrm{non-sec}}_{+\frac{1}{2},\,+1} - E^{\mathrm{non-sec}}_{+\frac{1}{2},\,0}\right) - \left(E^{\mathrm{non-sec}}_{-\frac{1}{2},\,+1} - E^{\mathrm{non-sec}}_{-\frac{1}{2},\,0}\right)$$
$$= \left(\left(3\cos(\beta_{\mathrm{dip}})^2 - 1\right) - 3\delta_{\mathrm{ZFS}}\sin(2\beta_{\mathrm{dip}})\right)\omega_{\mathrm{dip}}, \tag{36}$$

$$\omega^{\mathrm{non-sec}}_{-\frac{1}{2}\to+\frac{1}{2},\,0\leftrightarrow-1} = \left(E^{\mathrm{non-sec}}_{-\frac{1}{2},\,+1} - E^{\mathrm{non-sec}}_{-\frac{1}{2},\,0}\right) - \left(E^{\mathrm{non-sec}}_{+\frac{1}{2},\,0} - E^{\mathrm{non-sec}}_{+\frac{1}{2},\,-1}\right)$$
$$= -\left(\left(3\cos(\beta_{\mathrm{dip}})^2 - 1\right) - 3\delta_{\mathrm{ZFS}}\sin(2\beta_{\mathrm{dip}})\right)\omega_{\mathrm{dip}}. \tag{37}$$

It can be seen again that the ZFS leads to a shift in the dipolar frequencies. This shift is, besides the factor of 3, identical to the one that was obtained for the LaserIMD frequencies $\omega^{\mathrm{non-sec}}_{+1}$ and $\omega^{\mathrm{non-sec}}_{-1}$. From here, the next step is again the averaging over the orientations of the transient triplet label and the dipolar coupling vector that contribute to the LiDEER signal. However, this is even more complicated than it was in LaserIMD where all orientations are evenly excited by the laser-flash.

5   In LiDEER the triplet spins are also excited by microwave pulses who typically have a bandwidth that is much more narrow than the EPR spectrum of the transient triplet label. For example, the frequently used porphyrin labels have an EPR spectrum that is over 2 GHz broad (Di Valentin et al., 2014) of which a typical rectangular microwave pulse with a length of 10 ns can only excite roughly 120 MHz (Schweiger and Jeschke, 2001). Therefore, not all orientations of the transient triplet labels contribute to the LiDEER signal and it is rather tedious to even derive an expression for the integrals that describe the

10   orientation averaging. To circumvent this problem, the LiDEER traces will be calculated by time-domain simulations with weak microwave pulses in the next sections.

3 Materials and methods

3.1 Simulations

The powder averages for LaserIMD were performed by a numerical integration of Eq. (25) -(27) with home-written MATLAB

15   (version 2020b) scripts. For the angle β_{dip} a linear, equidistant grid from 0 to $\frac{\pi}{2}$ was used. Each value was weighted proportional to $\sin(\beta_{\mathrm{dip}})$. For the orientation of the transient triplet label, a grid with all three Euler angles α_{T}, β_{T} and γ_{T}, including the corresponding weights, was calculated according to the REPULSION approach (Bak and Nielsen, 1997; Hogben et al., 2011) with the software package *Spinach* (Hogben et al., 2011). To check for a sufficient convergence, a test run with

an increasing numbers of points for the two grids was simulated. The test run was stopped when the relative change $\Delta\epsilon$ in the simulated signal, when the number of grids points was increased, was below 1 %. For β_{dip} a grid size of 200 points was sufficient, whereas for α_T, β_T and γ_T 12800 points were necessary. For details of the convergence behavior, see S3.

The time-domain simulations for LiDEER were performed with *Spinach* (Hogben et al., 2011). The powder averaging was

5   done with the same grids that were used for LaserIMD. For details see S7.

3.2 Experiments and data analysis

LaserIMD and LiDEER measurements were performed on the two peptides TPP-pAA$_5$-NO• and TPP-pAA$_{10}$-NO• shown in Figure 3. They were purchased from Biosynthan (Berlin) as powder samples and used without further purification. They were dissolved in MeOD/D$_2$O (98/2 vol.%) and prior to freezing in liquid nitrogen, they were degassed with three freeze-pump-

10 thaw cycles. Light excitation was performed at a wavelength of 510 nm by an Nd:YAG laser system from Ekspla (Vilnius) that was coupled into the resonator via a laser fiber. EPR measurements were performed on a commercial Bruker E580 spectrometer, X-band measurements in an ER4118X-MS3 resonator and Q-band measurements in an ER5106QT-2 resonator. In X-band the resonator was critically coupled to a Q-value of $\approx$ 900-2000 for higher sensitivity and in Q-band it was overcoupled to a Q-value of $\approx$ 200. LaserIMD was recorded with the pulse sequence $\pi/2 - \tau - \pi - t$ - laser pulse - (τ-t) - echo

15 (Hintze et al., 2016). A 2-step phase cycle was implemented for baseline correction. Signal averaging was done by recording 10 shots per point. The zero-time correction was performed by recording a short reLaserIMD trace as reported in (Scherer et al., 2022). LiDEER measurements were performed with the pulse sequence: laser pulse $-$ DAF $- \pi/2 - \tau_1 - \pi - t - \pi -$ pump $-$ ($\tau_1 + \tau_2 - t$) $- \pi - \tau_2 -$ echo (Di Valentin et al., 2014). The delay-after-flash (DAF) was set to 500 ns and τ_1 to 400 ns. Nuclear modulation averaging was performed by varying the τ_1 time in 8 steps with $\Delta\tau_1 = 16$ ns. Phase cycling was performed with an

20 8-step scheme ((x) [x] xp x) as proposed by (Tait and Stoll, 2016). The LiDEER data were analysed with the python software package *DeerLab* (version 0.13.2) (Fábregas Ibáñez et al., 2020) and *Python* 3.9 with the DEER kernel $K_{DEER}(t, r)$ and Tikhonov regularization. A 3D homogenous background function was used and the regularization parameter was chosen according to the Akaiki information criterion (Edwards and Stoll, 2018). The validation was performed with bootstrapping by analyzing 1000 samples that are generated with artificial noise. The error was then calculated as the 95% confidence interval.

25 Further details can be found in S7 and S10.
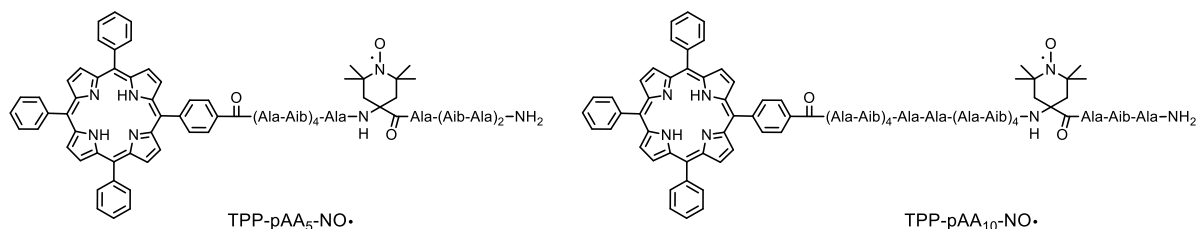
Figure 3: Chemical structures of the peptides TPP-pAA$_5$-NO• and TPP-pAA$_{10}$-NO• with the letter code Ala: L-alanine and Aib: α-isobutyric acid.

4 Results and Discussion

4.1 LaserIMD simulations

An initial simulation to study the effect of the ZFS in LaserIMD was performed for X-band ($\omega_T = 9.3$ GHz) with a dipolar coupling that corresponds to a distance of $r = 2.2$ nm, a ZFS of $D = 1159$ MHz and $E = -238$ MHz and zero-field

5   populations $P_x = 0.33$, $P_Y = 0.41$ and $P_Z = 0.26$. The ZFS and zero-field populations correspond to the porphyrin derivative TPP that is often used to perform LaserIMD and LiDEER measurements (Di Valentin et al., 2014; Hintze et al., 2016; Di Valentin et al., 2016; Bieber et al., 2018; Bertran et al., 2020). For simplicity, a complete excitation of the transient triplet label ($\gamma = 1$) was assumed and effects of the background were ignored ($B(t) = 1$). For a more detailed analysis, the contributions from the three coherence transfer pathways with $\Delta m_T = 1, 0, -1$, termed $V_{+1}^{\text{non-sec}}(t)$, $V_0^{\text{non-sec}}(t)$ and $V_{-1}^{\text{non-sec}}(t)$, are

10   simulated separately and presented in Figure 4 together with their resulting sum $V_{\text{LaserIMD}}^{\text{non-sec}}(t)$. They are also compared with the corresponding traces from the secular approximation $V_{\text{LaserIMD}}^{\text{sec}}(t)$, $V_{+1}^{\text{sec}}(t)$, $V_0^{\text{sec}}(t)$ and $V_{-1}^{\text{sec}}(t)$, where the ZFS is ignored. The comparison of the traces including and excluding the ZFS ($V_{+1}^{\text{non-sec}}(t)$ and $V_{-1}^{\text{non-sec}}(t)$ with $V_{+1}^{\text{sec}}(t)$ and $V_{-1}^{\text{sec}}(t)$) in Figure 4a and c shows that there is no visible effect of the ZFS in the traces $V_{+1}^{\text{non-sec}}(t)$ and $V_{-1}^{\text{non-sec}}(t)$ and they look virtually identical to $V_{+1}^{\text{sec}}(t)$ and $V_{-1}^{\text{sec}}(t)$. The frequency shift $\delta_{\text{ZFS}} \sin(2\beta_{\text{dip}}) \omega_{\text{dip}}$ seems to be averaged out after integration

15   for this terms. The situation is different in the case of $V_0^{\text{non-sec}}(t)$ and $V_0^{\text{sec}}(t)$ in Figure 4b. Whereas $V_0^{\text{sec}}(t)$ is a constant function of time and does not contribute to the echo modulation, $V_0^{\text{non-sec}}(t)$ shows a continuous decay of the echo intensity with increasing time. This decay does not contain any additional dipolar oscillations and its shape does not seem to follow any obvious simple mathematical law. For the full LaserIMD traces in Figure 4d, this means that, whereas without taking ZFS into account the trace $V_{\text{LaserIMD}}^{\text{sec}}(t)$ looks like a $S = 1/2$ DEER trace with and a modulation depth of $\lambda = 66.\bar{6}$ %. , the trace

20   $V_{\text{LaserIMD}}^{\text{non-sec}}(t)$ with the ZFS shows the same dipolar oscillations but on top of a decay. This also means that, due to the coherence transfer pathway with $\Delta m_T = 0$ also resulting in a variation of the echo intensity, the modulation depth of LaserIMD is increased by the ZFS and values higher than $66.\bar{6}$ %. can be reached.
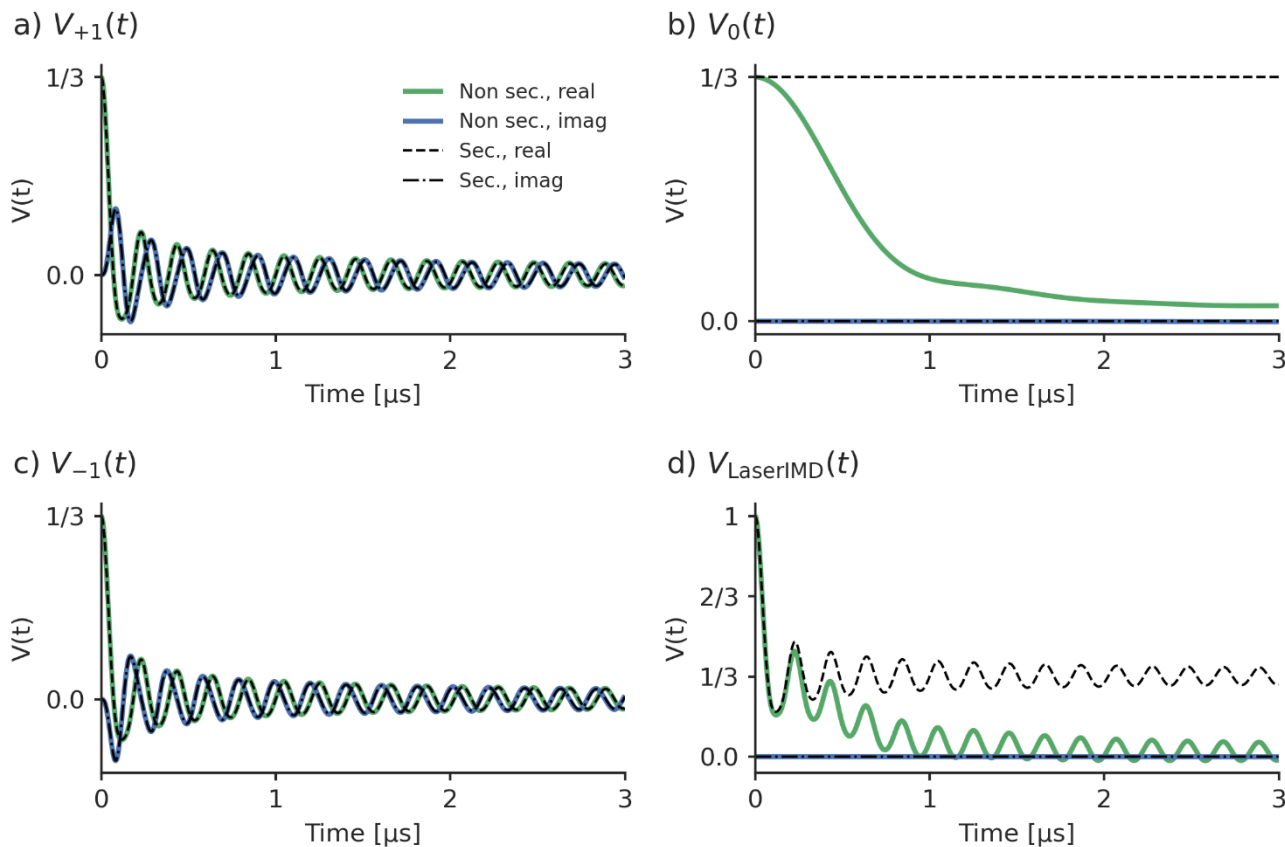
Figure 4: Comparison of simulated LaserIMD traces with and without non-secular interactions with the values $D = 1159$ MHz, E= -238 MHz and $P_x = 0.33$, $P_y = 0.41$ and $P_z = 0.26$, $\omega_T = 9.3$ GHz (X-band) and $r = 2.2$ nm. a) $V_{+1}^{\text{non-sec}}(t)$, b) $V_0^{\text{non-sec}}(t)$, c) $V_{-1}^{\text{non-sec}}(t)$, d) $V_{\text{LaserIMD}}^{\text{non-sec}}(t) = V_{+1}^{\text{non-sec}}(t) + V_0^{\text{non-sec}}(t) + V_{-1}^{\text{non-sec}}(t)$.

5 The frequency shift caused by the non-secular terms of the ZFS in LaserIMD depends not only on D and E, but also on the zero-field populations P_x, P_y and P_z, the Zeeman frequency ω_T and the distance r (see Eq. (21) -(24)). The influence of these parameters was studied by simulating additional LaserIMD traces with different ZFSs, zero-field populations, magnetic fields and distances (see Figure 5). In Figure 5a, two LaserIMD traces in X- and Q-band ($\omega_T = 9.3$ GHz and $\omega_T = 34.0$ GHz) with TPP as a transient triplet label and a distance of $r = 2.2$ nm are compared. Figure 5b shows the comparison between the ZFS

10 of TPP ($D = 1159$ MHz and E= -238 MHz) and a stronger ZFS of $D = 3500$ MHz and E= -800 MHz, as such high values are possible for some labels (Williams et al., 2020). Both simulations were performed in Q-band with $r = 2.2$ nm. In Figure 5c, the effect of different distances of $r = 2.2$ nm and $r = 5$ nm on $V_0^{\text{non-sec}}(t)$ is shown for TPP in Q-band. Figure 5d shows three simulations with the population of the zero-field triplet states spin being completely assigned to either P_x, P_y or P_z.

Figure 5a, Figure 5b and Figure 5d show that there are no visible differences in the dipolar oscillations in $V_{+1}^{\text{non-sec}}(t)$ and

15 $V_{-1}^{\text{non-sec}}(t)$, when the Zeeman frequency, ZFS or zero-field populations are changed. This can also be seen in the SI in S4,

S5 and S6 where the traces for different Zeeman frequencies, ZFSs and distances are compared in more detail. This fits to the former results in Figure 4 that the frequency shift due to the ZFS is virtually averaged out in a powder sample for $V_{+1}^{\text{non-sec}}(t)$ and $V_{-1}^{\text{non-sec}}(t)$, so changing the involved parameters should also have little effect. The situation is different for $V_0^{\text{non-sec}}(t)$, which, as it is shown in Figure 4c, feels a stronger effect of the ZFS. The previously mentioned decay is faster for a lower

5 Zeeman frequencies (see Figure 5a) and a stronger ZFS (see Figure 5b). Because δ_{ZFS} ultimately depends on the ratio of the ZFS to the Zeeman frequency, a higher ZFS and a lower Zeeman frequency both increase the magnitude of the frequency shift of $\omega_0^{\text{non-sec}}$ in the same way which leads to the same effect on the LaserIMD trace. Figure 5c shows that shorter distances also lead to a faster decay of $V_0^{\text{non-sec}}(t)$. As can be seen in Eq. (21) -(23), changing the distances from 2.2 to 5 nm leads to a rescale of the LaserIMD frequencies $\omega_{+1}^{\text{non-sec}}$, $\omega_0^{\text{non-sec}}$ and $\omega_{-1}^{\text{non-sec}}$ with r^{-3}. This distance dependency of the dipolar

10 oscillations (not shown in Figure 5c) is used in PDS for the calculation of the distance distributions. In the case of LaserIMD, the steepness of the decay of $V_0^{\text{non-sec}}(t)$ is an additional feature that depends on the distance between the spin labels. The parameters that have the least influence on the LaserIMD trace are the zero-field populations (see Figure 5d). Changing the populations of the zero-field states does not seem to affect the dipolar oscillations, as it was the case for different ZFSs and magnetic field strengths. This time, also the decay of $V_0^{\text{non-sec}}(t)$ is barely affected by different zero-field populations.

15 Taken together, variation in the ZFS parameter, the population of the ZFS states and the employed magnetic field (X- or Q-band) do not affect the dipolar oscillations in $V_{+1}^{\text{non-sec}}(t)$ and $V_{-1}^{\text{non-sec}}(t)$. They mostly have an effect on the decay of $V_0^{\text{non-sec}}(t)$, such that a stronger ZFS parameters and lower magnetic fields will lead to a stronger additional decay in the LaserIMD trace. The additional decay is also stronger for shorter distances between the spin labels and can therefore be used as a source for the calculation of the distance distribution.
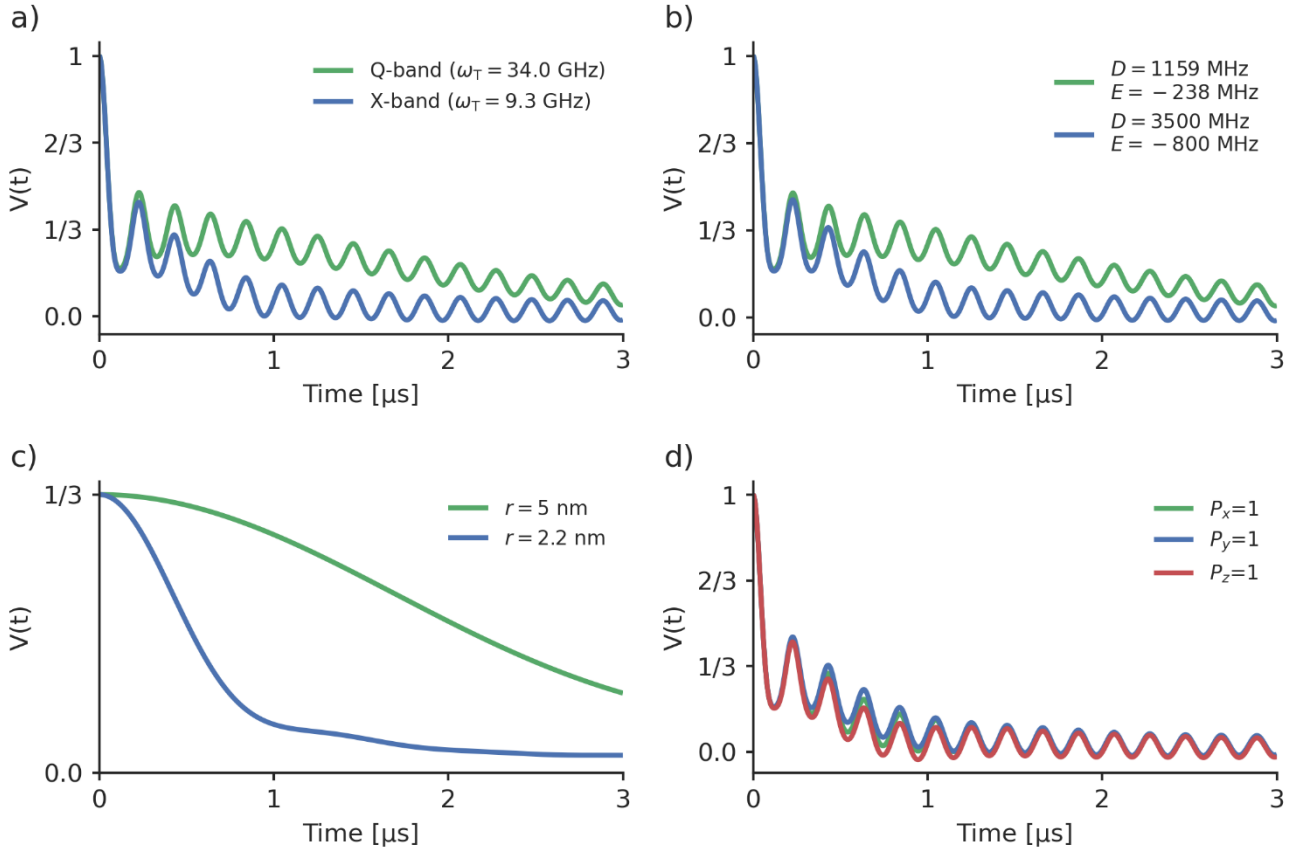
Figure 5: A comparison of different LaserIMD traces $V_{\text{LaserIMD}}^{\text{non-sec}}(t)$ with different parameters. The following values were used for the simulations. a) TNPP, $r = 2.2$ nm and $\omega_T = 34$ GHz (green) and $\omega_T = 9.3$ GHz (blue) b) $P_x = 0.33$, $P_y = 0.41$, $P_z = 0.26$, $r = 2.2$ nm, $\omega_T = 9.3$ GHz and $D = 1159$ MHz, E= -238 MHz (green) and $D = 3500$ MHz, E= -800 MHz (blue) c) TPP, $\omega_T = 34$ GHz and $r = 2.2$ nm green) and $r = 5$ nm (blue) d) $D = 1159$ MHz, E= -238 MHz $r = 2.2$ nm, $\omega_T = 9.3$ GHz and $P_x = 1$, $P_y = 0$, $P_z = 0$ (green), $P_x = 0$, $P_y = 1$, $P_z = 0$ (blue) and $P_x = 0$, $P_y = 0$, $P_z = 1$ (red).

So far, all simulations only showed a visible effect of the ZFS on $V_0^{\text{non-sec}}(t)$, no significant influence on $V_{+1}^{\text{non-sec}}(t)$ and $V_{-1}^{\text{non-sec}}(t)$ was observed. To check if and when the ZFS has also an influence on $V_{+1}^{\text{non-sec}}(t)$ and $V_{-1}^{\text{non-sec}}(t)$, we performed additional simulations where the effect of the ZFS is expected to be stronger. This can be obtained by either lower Zeeman frequencies or higher ZFS values. As the effect on δ_{ZFS} is the same in both cases, the ratio of D and the Zeeman frequency of the triplet ω_T can be defined as:

$$q = \frac{D}{\omega_T} \tag{38}$$

For simplification, the ZFS was assumed to be axial with $E = 0$. This simplifies the expression of δ_{ZFS} to:

$$\delta_{\text{ZFS}} = \frac{3}{4} q \sin(2\beta_{\text{T}}) \cos(\alpha_{\text{T}}) \tag{39}$$

The simulation in X-band with TPP from Figure 4 corresponds to a ratio where q is approximately 0.13. Here, we tried values for q of up to 1. Figure 6 shows the sum of $V_{+1}^{\text{non-sec}}(t)$ and $V_{-1}^{\text{non-sec}}(t)$ of these simulations and compares it to a trace where the effect of the ZFS has been ignored. It can be seen that up to $q = 0.5$, the traces are negligibly affected by the ZFS. For higher values, the dipolar oscillations start to get shifted to slightly higher frequencies and are also smoothed out more quickly.

5   Analyzed with the over-simplified kernel $K_{\text{DEER}}(t,r)$ of the $S = 1/2$ model, this would result in a shift to smaller distances and an artificial broadening of the distance distribution. However, as $q = 1$ is equivalent to a ZFS that is in the same order of magnitude as the Zeeman frequency, this is not relevant for most practical applications, as LaserIMD is typically performed at X- or Q-band ($\omega_{\text{T}} = 9.3$ GHz or $\omega_{\text{T}} = 34.0$ GHz) and all transient triplet labels used so far have a ZFS value D below 4 GHz (Dal Farra et al., 2019b; Williams et al., 2020). Even in the most extreme case, this would result in values for q smaller than

10   0.5. Consequently, this effect is not relevant for most experiments and even though the contributions from $V_{+1}^{\text{non-sec}}(t)$ and $V_{-1}^{\text{non-sec}}(t)$ can in principle by influenced by the ZFS, it seems to be a safe assumption that the ZFS in LaserIMD affects only the decay in $V_0^{\text{non-sec}}(t)$ and not the dipolar oscillations in $V_{+1}^{\text{non-sec}}(t)$ and $V_{-1}^{\text{non-sec}}(t)$.
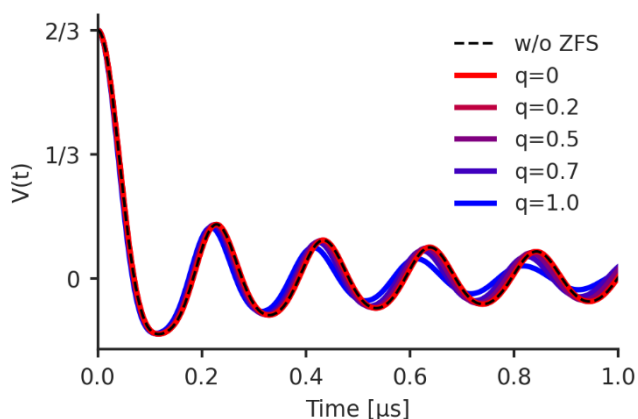
Figure 6: a) The sum of $V_{+1}^{\text{non-sec}}(t)$ and $V_{-1}^{\text{non-sec}}(t)$ for different values of q and $P_x = 0.33$, $P_y = 0.41$, $P_z = 0.26$ and $r = 2.2$ nm. Only

15   the real part is shown.

As was stated before, in the secular approximation, LaserIMD traces can be analysed with the kernel $K_{\text{DEER}}(t,r)$ of the $S = 1/2$ model. To check to what extend this is true when the ZFS is not negligible, we simulated LaserIMD traces that were subsequently analyzed with $K_{\text{DEER}}(t,r)$. To mimic experimental condition more closely, we assumed an incomplete excitation of the transient triplet label and the intermolecular dipolar background was also considered. TPP was used as transient triplet

20   label with a distance to the permanent spin label of $r = 2.2$ nm and a modulation depth of $\lambda = 50\%$, which roughly correspond to the values that can be typically achieved in experiments. Simulations were performed in X- and Q-band with

different background decay rates varying between $k = 0.0\ \mu\text{s}^{-1}$ (no background) to $k = 0.4\ \mu\text{s}^{-1}$. The resulting traces were then analyzed with $K_{\text{DEER}}(t, r)$ and Tikhonov regularization (see details in S7).
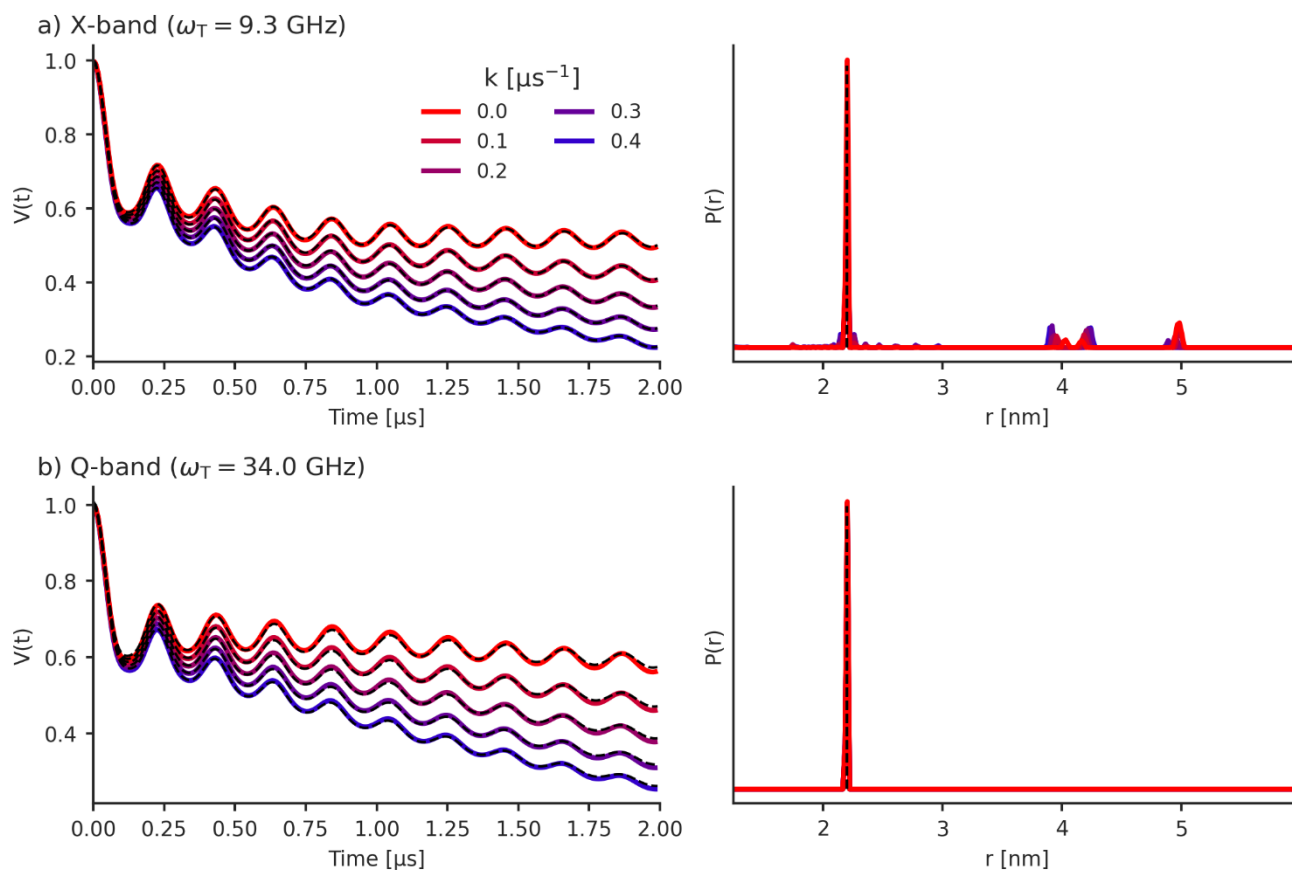
Figure 7: Simulations LaserIMD traces $V^{\text{non-sec}}_{\text{LaserIMD}}(t)$ including the non-secular terms for TPP as transient triplet label and $r = 2.2$ nm in a) X-band ($\omega_{\text{T}} = 9.3$ GHz) and b) Q-band ($\omega_{\text{T}} = 34.0$ GHz). The background decay was varied between $k = 0.0\ \mu\text{s}^{-1}$ and $k = 0.4\ \mu\text{s}^{-1}$. The left side shows the simulated traces (with the fits as dashed black line) and the right side shows the distance distributions that were obtained with Tikhonov regularization with $K_{\text{DEER}}(t, r)$. The true distance of $r = 2.2$ nm is plotted as dashed black line.

Table 1: The background decay values and modulation depths that were determined for the simulations from Figure 7. The modulation depth for the simulations was always set to $\lambda = 50\,\%$.

$k\ [\mathrm{\mu s^{-1}}]$	X-band ($\omega_T = 9.3\,\mathrm{GHz}$)		Q-band ($\omega_T = 34.0\,\mathrm{GHz}$)	
	$k_{\mathrm{fit}}\ [\mathrm{\mu s^{-1}}]$	$\lambda_{\mathrm{fit}}\ [\%]$	$k_{fit}\ [\mathrm{\mu s^{-1}}]$	$\lambda_{\mathrm{fit}}\ [\%]$
0.0	0.00	47	0.07	32
0.1	0.00	54	0.17	32
0.2	0.00	61	0.26	33
0.3	0.00	66	0.35	34
0.4	0.01	70	0.44	36

The simulations and fitted distance distributions can be seen in Figure 7 and the background decay rates and modulations depths that were obtained by the fits in Table 1. Figure 7 shows that the fits agree well with the simulated data and the main

5 peak of the distance distribution at $r = 2.2$ nm is fitted appropriately in X- as well as in Q-band. However, there can be additional artefact peaks in the distance distributions, and the fitted modulation depths and background decay rates can be erroneous (see Table 1). This is particularly pronounced in X-band, which shows artefacts in the distance distribution between 3.9 nm and 5 nm and at the higher distance end. Moreover, the background decay rates and modulation depths deviate significantly from the values that were originally used for the simulations. The simulations in X-band are always fitted with a

10 background decay rate close to zero ($k_{\mathrm{fit}} \approx 0.0\,\mathrm{\mu s^{-1}}$), even in the cases where the strongest background was included ($k = 0.4\,\mathrm{\mu s^{-1}}$) in the simulation. The modulation depth was fitted with values from 47 % to 70 % and varies significantly for different background decays. In Q-band, the fitted parameters correspond closer to the input values of the simulations. The distance artefacts that appeared in X-band between 3.9 nm and 5 nm have disappeared, and only those at the long distance limit remain. The obtained background decay rates correspond better with the true values, but are always larger as them. Only

15 the obtained modulation depths are less accurate than in X-band and fitted to values between 32 % and 36 %. Even though, these simulations are only anecdotal evidence and generalizations from these data must be taken with caution, they show that when LaserIMD data are analysed with $K_{\mathrm{DEER}}(t, r)$ it is possible to extract the main distance peak correctly. Analyzing LaserIMD traces with $K_{\mathrm{DEER}}(t, r)$ can thus an option in situations where the ZFS values and zero-field populations of the transient triplet label are unknown and their effect cannot be included in the analysis. However, this way of analyzing

20 LaserIMD data can give artefacts at higher distances and also errors in the obtained modulation depth and background decay rate. This is particularly pronounced for low magnetic fields (e.g. X-band) and similar results can be expected for transient triplet labels with higher ZFS values.

4.2 LiDEER simulations

In LaserIMD, transient triplet labels of all orientations are excited by the laser flash and contribute to the signal, thus an integration over all corresponding Euler angles needs to be performed (Eq. (25) -(27)). Contrary to that, in LiDEER the transient triplet labels are additionally excited by microwave observer pulses. As the spectrum of many transient triplet labels

5 exceeds the excitation bandwidth of these pulses (Di Valentin et al., 2014; Williams et al., 2020; Krumkacheva et al., 2019), only a small number of orientations within the excitation bandwidth contribute to the signal. As the LiDEER frequencies (Eq. (34) -(37)) depend on the orientation of the transient triplet label when the ZFS is included, the trace should change when the observer pulse excites different parts of the spectrum. For some orientations, the frequency shift due to the ZFS vanishes and the LiDEER frequencies are identical to the DEER frequencies. One example thereof are the canonical orientations X, Y and

10 Z, because the Euler angles for these orientations are $\beta_T = \frac{\pi}{2}$ and $\gamma_T = 0$ for the X-orientation, $\beta_T = \frac{\pi}{2}$ and $\gamma_T = \frac{\pi}{2}$ for the Y-orientation and $\beta_T = 0$ and $\gamma_T = 0$ for the Z-orientation (Richert et al., 2017) and according to Eq. (24) $\delta_{ZFS} = 0$ for these angles. In experiments, when the commonly used nitroxides or other spin labels with $g_D \approx 2$ are used as pump spin, the resonator bandwidth allows to use only the $Y^\pm$ peaks as observer position, because the other parts of the spectrum lie outside the resonator profile (Bieber et al., 2018). Noteworthy, in the powder case, there are several orientations that contribute to the

15 $Y^\pm$ peaks (Richert et al., 2017), not only the Y-orientation, and an influence of the ZFS cannot be excluded for all of them. Therefore, to study the effect of the ZFS in LiDEER, numerical time-domain simulations for different ZFS values in X- and Q-band were performed. The traces were then analyzed with $K_{DEER}(t,r)$ and Tikhonov regularization to check for artefacts in the thereby obtained distance distributions. The microwave pulses were placed on the Y^+ peak of the EPR-spectrum and had a finite length, power and bandwidth so that only the parts of the spectrum around the Y^+ peak contribute to the signal, as it is

20 the case in the experimental setup. A simulation for TPP as transient triplet label was performed in X- and Q-band and an additional simulation with a larger ZFS of $D = 3500$ MHz and $E = -800$ MHz was performed in X-band. The permanent spin label was included as a doublet spin with an isotropic g-value ($g_D = 2$) and without any additional hyperfine interactions. The distance was set to $r = 2.2$ nm and no background from intermolecular spins was included. The details of the calculation of the distance distribution in S7 and the details of the simulations can be found in S8.
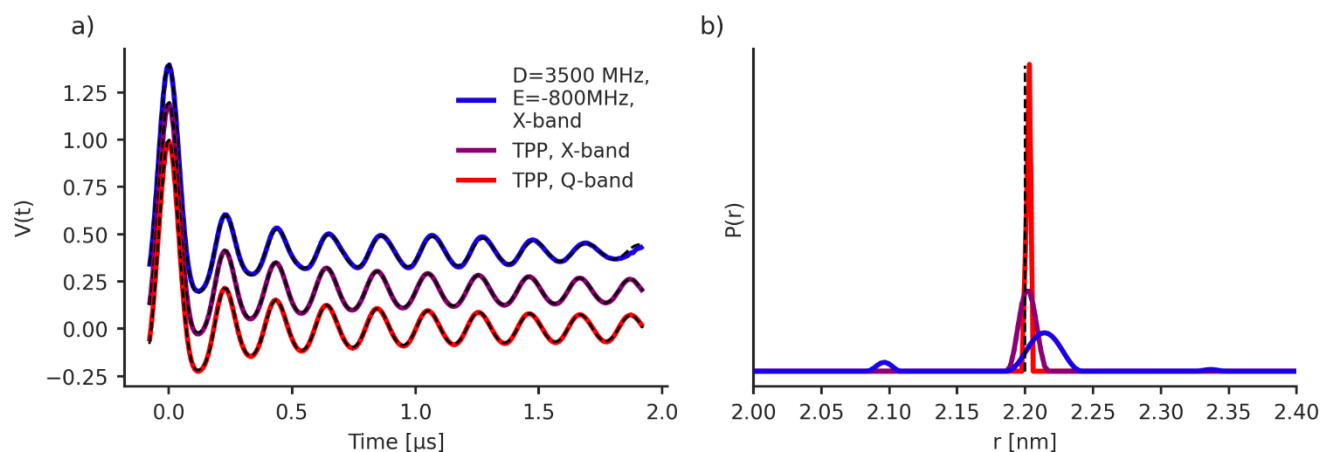
Figure 8: a) LiDEER simulations with the observer pulse placed on the Y^+-peak of the EPR spectrum of the transient triplet label in different frequency bands and with different ZFS. The traces are shifted by 0.2 for better visibility. For Q-band and TPP, the magnetic field was set to 1.2097 T and the observer frequency to 33.646 GHz; for X-band, the magnetic field was set to 0.33 T, which for TPP corresponds to an observer frequency of 9.042 GHz and for a ZFS with $D = 3500$ MHz and $E = -800$ MHz to an observer frequency of 9.042 GHz. The further parameters were $P_x = 0.33$, $P_y = 0.41$, $P_z = 0.26$ and $r = 2.2$ nm. The numerical simulations were fitted with Tikhonov regularization. The fits are shown as dashed black lines. b) The corresponding distance distribution. The true distance of $r = 2.2$ nm is plotted as dashed black line.

Figure 8a shows the simulated LiDEER traces and Figure 8b the obtained distance distributions. The differences in the LiDEER traces for different ZFS and Zeeman frequencies are smaller than they are in LaserIMD (Figure 4). This is because in LiDEER, there is no equivalence for the coherence transfer pathway with $\Delta m_T = 0$ that showed the strongest dependency on the ZFS and magnetic fields in LaserIMD (Figure 5). The distance distribution for TPP in Q-band shows a narrow peak at 2.20 nm with a full width at half maximum (FWHM) of 0.004 nm. This fits to the 2.20 nm (FWHM $= 0$ nm) that were used for the simulation. In X-band, the distance distribution with TPP is also centered at 2.20 nm, but gets broadened to a FWHM of 0.014 nm. This trend increases for the large ZFS with $D = 3500$ MHz and $E = -800$ MHz in X-band. Here, the distance distribution gets even broader with an FWHM of 0.028 nm and is now also shifted to a center of ≈ 2.22 nm. This behavior fits to the results of LaserIMD in Figure 6, where the shifts of the dipolar oscillation get also larger when the ZFS is large compared to the Zeeman frequency. However, it must also be stated that the observed shifts of the distance distribution are still rather small here and should be below the resolution limit that is relevant in most experiments. Additional traces, where the observer pulse is set off-resonance to the canonical peaks were also performed and are presented in S9. Here, especially for the case of $D = 3500$ MHz and $E = -800$ MHz in X-band, the dipolar trace show more significant differences from the case with excitation off the Y^+ peak. The dipolar oscillations fade out much faster, which also leads to a stronger broadening of the distance distributions.

This means that in general the ZFS has an effect on LiDEER and the LiDEER trace changes, when different parts of the EPR-spectrum of the transient triplet label are used for excitation by the observer pulses. However, in the special case when either of the $Y^\pm$ peaks is used as position for the observer pulse, the effect of the ZFS can be suppressed and LiDEER traces can be

analysed with the $K_{\mathrm{DEER}}(t,r)$ kernel without introducing significant artefacts in the distance distribution. The is particularly true for TPP -and other transient triplet labels with a similar ZFS- in Q-band.

4.3 Experiments

To experimentally confirm the theoretical finding that the ZFS has an influence on the shape of the LaserIMD trace, LaserIMD

5 measurements were performed at different magnetic field strengths at X- and Q-band and with two model systems with a shorter and longer distances between the labels. This should result in scenarios were the ZFS has either a weak effect on the trace (high magnetic field strength and long distance) or strong effect (low magnetic field strength and short distance). The LaserIMD experiments were simulated with the newly derived model that includes the ZFS. The distance distributions and background decay rates that were used for these simulations of the LaserIMD traces were determined with LiDEER. The

10 measurements were performed with the peptides TPP-pAA$_5$-NO• and TPP-pAA$_{10}$-NO•. They contain TPP as transient triplet label and the nitroxide TOAC as permanent spin label. Both labels are separated by a rather rigid helix consisting of L-alanine and α-isobutyric acid (Di Valentin et al., 2016).
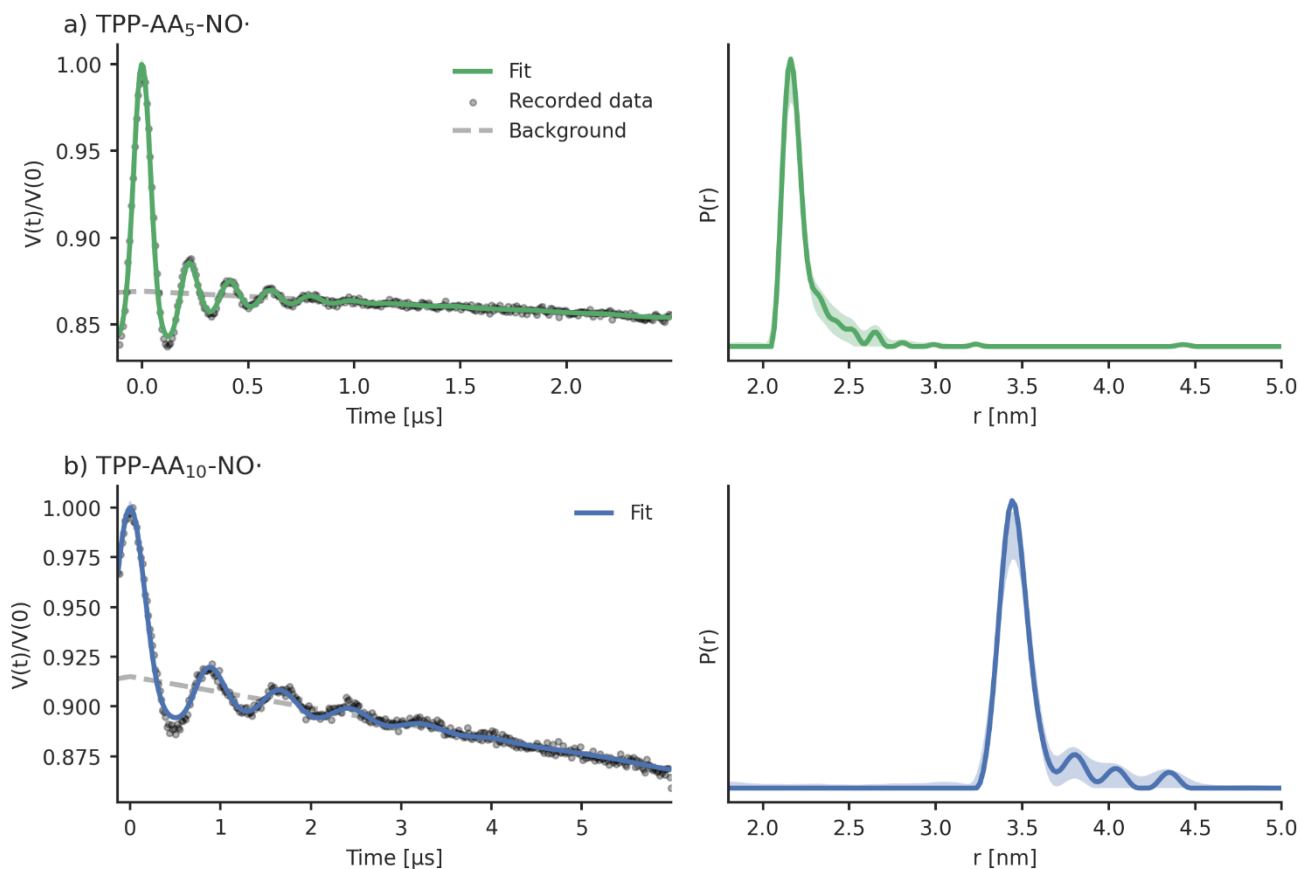
Figure 9: Experimental LiDEER data of the two peptides, all recorded in Q-band at 30 K in MeOD/D$_2$O (98/2 vol.%). a) TPP-pAA$_5$-NO• and b) TPP-pAA$_{10}$-NO•. The raw data are depicted on the left side as grey dots with the fits as straight line, the background fit is depicted as dashed grey line. The distance distributions obtained with Tikhonov regularization (Fábregas Ibáñez et al., 2020) is shown on the right side. The shaded areas correspond to the 95% confidence intervals that were obtained with bootstrapping.

So far, the LaserIMD simulations that were described above did only invoke a single delta-like distance. To simulate LaserIMD for an entire distance distribution, the dipolar kernel $K_{\text{LaserIMD}}^{\text{non-sec}}(t,r)$ needs to be calculated. Therefore, we implemented a C++ software tool that can perform the numerical integration of Eq. (25)-(27) to calculate $S_{\text{LaserIMD}}^{\text{non-sec}}(t,r)$. It allows the user to specify different ZFS values, zero-field populations and Zeeman frequencies. The background decay and modulation depth can then be included afterwards to obtain the full Kernel $K_{\text{LaserIMD}}^{\text{non-sec}}(t,r)$ (see Eq. (29)). The program including its source-code is available at github (https://github.com/andreas-scherer/LaserIMD_kernel). Here, it was used to calculate the kernel that corresponds to the experimentally determined parameters for TPP of the peptides TPP-pAA$_5$-NO• and TPP-pAA$_{10}$-NO• (ZFS values: $D = 1159$ MHz and $E = -238$ MHz and zero-field populations: $P_x = 0.33$, $P_Y = 0.41$ and $P_Z = 0.26$ (Di Valentin et al., 2014)) at the Zeeman frequencies that correspond to the used magnetic field strengths ($\omega_T = 9.28$ GHz, $\omega_T = 9.31$ GHz in X-band and $\omega_T = 34.00$ GHz in Q-band, see also S9). The distance distributions of TPP-pAA$_5$-NO• and TPP-pAA$_{10}$-NO•

that were used for the LaserIMD simulations were obtained by LiDEER measurements. LiDEER traces were recorded in Q-band with the observer pulse placed on the Y⁻ peak and analyzed with $K_{\text{DEER}}(t,r)$ and Tikhonov regularization, as the simulations in section 4.2 showed that no artefacts are to be expected in this case. More details on the experiments and distance calculations can be found in S7 and S10. The results of the LiDEER measurements are shown in Figure 9 and the extracted

5   distance distributions exhibit a narrow peak at 2.2 nm for TPP-pAA$_5$-NO• and at 3.5 nm for TPP-pAA$_{10}$-NO• as expected (Bieber et al., 2018; Di Valentin et al., 2016). As the LaserIMD and LiDEER measurements have different modulation depths, the modulation depth of LiDEER λ_{LiDEER} cannot be used for the simulation of the LaserIMD. This makes the modulation depth of the LaserIMD traces $\lambda_{\text{LaserIMD}}$ the only parameter that is missing for the simulations. Therefore, the simulated LaserIMD traces were fitted to the measured ones by rescaling the modulation depth. As the background decay rate depends

10 linearly on the modulation depth (Hu and Hartmann, 1974; Pannier et al., 2000), it must be rescaled together with the modulation depth. For LaserIMD, we assume that coherence transfer pathways with $\Delta m_{\text{T}} = 0$ does not contribute to the background, as its decay of the echo intensity is on a much longer timescale than the dipolar oscillations that constitute the main contribution of the intermolecular background. Therefore, we additionally reduce the rescaled background decay rate by a factor of $2/3$:

$$K_{\text{LaserIMD}}^{\text{non-sec}}(t,r)_{\lambda_{\text{LaserIMD}}} = \exp\left(-\frac{2}{3}\frac{\lambda_{\text{LaserIMD}}}{\lambda_{\text{LiDEER}}}k_{\text{LiDEER}}t\right)\left(\lambda_{\text{LaserIMD}}S_{\text{LaserIMD}}^{\text{non-sec}}(t,r) + (1 - \lambda_{\text{LaserIMD}})\right) \tag{40}$$

$$V_{\text{LaserIMD}}(t)_{\lambda_{\text{LaserIMD}}} = K_{\text{LaserIMD}}^{\text{non-sec}}(t,r)_{\lambda_{\text{LaserIMD}}}P_{\text{LiDEER}}(r) \tag{41}$$

15 The simulated LaserIMD trace $V_{\text{LaserIMD}}(t)_{\lambda_{\text{LaserIMD}}}$ was fitted to the experimental LaserIMD data by varying the modulation depth $\lambda_{\text{LaserIMD}}$ so that the root-mean-square displacement of the simulated and experimental traces was minimized. Simulations without the effect of the ZFS were also performed in order to clearly see the difference to the simulations with the ZFS. For the simulations without the ZFS, the modulation depth of the LaserIMD simulations with the ZFS was taken as it was determined by the fit and reduced by a factor of $2/3$, because the coherence transfer pathway with $\Delta m_{\text{T}} = 0$ no longer

20 contributes to the echo modulation.
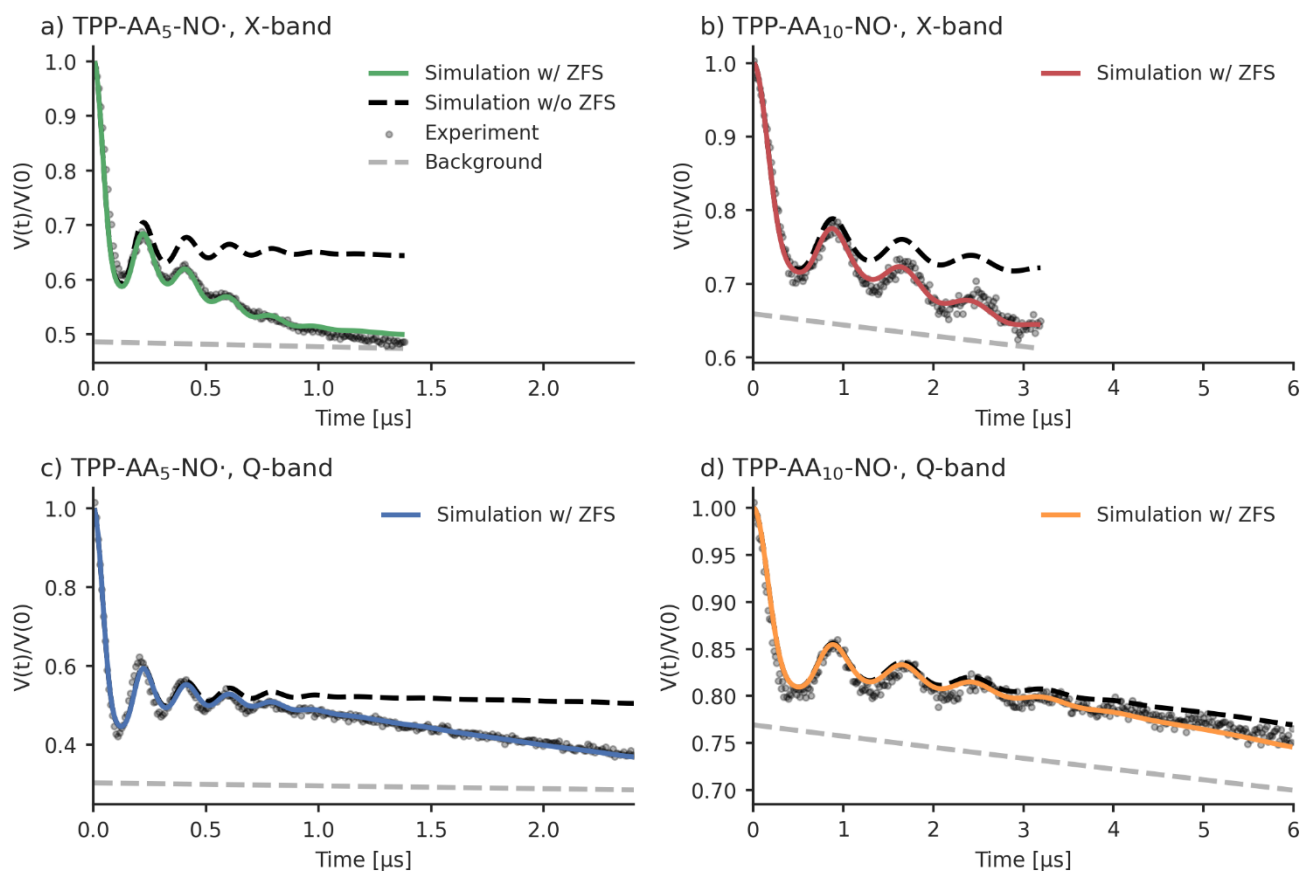
Figure 10: Experimental LaserIMD traces of the peptides, recorded at 30 K in MeOD/D$_2$O (98/2 vol.%). a) TPP-AA$_5$-NO• in X-band (ω_I = 9.28 GHz) (green), b) TPP-AA$_{10}$-NO• in X-band (ω_T = 9.31 GHz) (red), c) TPP-AA$_5$-NO• in Q-band (ω_T = 34.00 GHz) (blue), d) TPP-AA$_{10}$-NO• in Q-band (ω_T = 34.00 GHz) (orange). The colored traces show simulations that include the ZFS. The simulations without the effects of the ZFS are shown as black dashed line. The experimentally recorded data are depicted as grey dots. The backgrounds of the simulations are shown as grey dashed line. The simulations were performed with the distance distributions and background decays that were obtained by the LiDEER measurements.

The results of the LaserIMD measurements and the corresponding simulations are shown in Figure 10. It can be clearly seen that the shape of the experimental traces changes depending on whether they were recorded in X- or Q-band and with those with a stronger decay in X-band. This is a first strong indication of the effect of the ZFS, as predicted by the simulations (see Figure 5). The influence of the ZFS shows itself clearly in the differences between the experimental data and the simulations where the effect of the ZFS was ignored. In particular, the experimental LaserIMD traces show a stronger decay than the background decay of simulations without the ZFS. This difference is more pronounced in TPP-AA$_5$-NO• than in TPP-AA$_{10}$-NO• and also stronger in X-band than in Q-band. Thus, for TPP-AA$_5$-NO• in X-band, the deviation between the simulations without the ZFS and the experiments is the largest, whereas in the case of TPP-AA$_{10}$-NO• in Q-band, it is nearly absent. This additional decay of the experimental traces cannot be explained without considering the effect of the ZFS, but is properly

MAGNETIC RESONANCE
Discussions

understandable with a model that includes the ZFS. The stronger decay of the experimental traces can be assigned to the coherence transfer pathway with $\Delta m_\text{T} = 0$, which leads to an additional contribution to the LaserIMD trace $V_0^{\text{non-sec}}(t)$ with a continuously decaying signal (Figure 4). As shorter distances and lower magnetic fields lead to a stronger decay of $V_0^{\text{non-sec}}(t)$, this also explains why the additional decay in the experimental data is stronger for TPP-AA$_5$-NO• than for TPP-AA$_{10}$-NO• and stronger in X- than in Q-band. It is noteworthy that the model with the ZFS provides not only a qualitative but also a quantitative agreement between the experimentally recorded LaserIMD traces and the corresponding simulations.

5 Conclusion and Outlook

In light-induced PDS, the ZFS interaction of the transient triplet label is a crucial parameter that can alter the shape of the dipolar traces. This implies that in contrast to the former assumption, the spin system in LaserIMD and LiDEER cannot be treated in the secular approximation where the spin systems behaves as if it would consist of two $S = 1/2$ spins. A theoretical description of LaserIMD and LiDEER that also includes non-secular terms was developed and it was shown that the dipolar frequencies depend on the magnitude of the ZFS and the Zeeman frequency (i.e. the external magnetic field). Time-domain simulations showed that in LiDEER, this effects of the ZFS can be suppressed by exciting either of the $Y^\pm$ peaks with the observer pulses and by using transient triplet labels whose ZFS is small compared to the Zeeman frequency, like e.g. TPP in Q-band. In LaserIMD, simulations as well as experiments confirmed that there is an influence of the ZFS on the dipolar trace. It virtually does not affect the dipolar oscillation of the coherence transfer pathways with $\Delta m_\text{T} = \pm 1$, but is manifested in an additional decay of the LaserIMD trace. This decay is caused by the third coherence transfer pathway with $\Delta m_\text{T} = 0$, which was formerly believed not to contribute to the signal. The strength of this additional decay primarily depends on the ratio of the ZFS to the Zeeman frequency and also the distance between the transient and permanent spin label: It is stronger for larger ZFS, lower magnetic fields and shorter distances.

A software tool for the calculation of LaserIMD kernels that takes the influence of the ZFS into account was developed. It is available at github (https://github.com/andreas-scherer/LaserIMD_kernel) and allows to specify different ZFS, zero-field populations and Zeeman frequencies. The feasibility of the new kernel was proven by experimentally recorded LaserIMD traces. A kernel which ignores the ZFS cannot fit these traces correctly and strong derivations between the experimental data and simulations can be observed. With the newly developed model, however, excellent fits of the experimental data were produced. This shows that the ZFS can have a significant impact in LaserIMD and should be considered when experimental data are analyzed.

6 Data availability

The raw data can be downloaded at https://doi.org/10.5281/zenodo.7283499.

7 Code availability

The source code can be downloaded at https://github.com/andreas-scherer/LaserIMD_kernel.

8 Author contribution

AS and MD conceived the research idea and designed the simulations and experiments. AS performed the analytical calculations and AS and BY conducted the simulations and experiments and analyzed the results. AS prepared all the figures and wrote the draft manuscript. All authors discussed the results and revised the manuscript.

9 Competing interests

The authors declare no conflict of interests.

10 Acknowledgements

We thank Joschua Braun and Stefan Volkwein for helpful discussions concerning the numerical integration of the integrals for the LaserIMD kernel. This project has received funding from the European Research Council (ERC) under the European Union's Horizon 2020 research and innovation programme (Grant Agreement number: 772027 — SPICE — ERC-2017-COG). AS gratefully acknowledge financial support from the Konstanz Research School Chemical Biology (KoRS-CB).

11 References

Abdullin, D., Matsuoka, H., Yulikov, M., Fleck, N., Klein, C., Spicher, S., Hagelueken, G., Grimme, S., Luetzen, A., and Schiemann, O.: Pulsed EPR Dipolar Spectroscopy under the Breakdown of the High-Field Approximation: The High-Spin Iron(III) Case, Chemistry – A European Journal, 0, https://doi.org/10.1002/chem.201900977, 2019.

5 Bak, M. and Nielsen, N. C.: REPULSION, A Novel Approach to Efficient Powder Averaging in Solid-State NMR, Journal of Magnetic Resonance, 125, 132–139, https://doi.org/10.1006/jmre.1996.1087, 1997.

Bertran, A., Henbest, K. B., De Zotti, M., Gobbo, M., Timmel, C. R., Di Valentin, M., and Bowen, A. M.: Light-Induced Triplet–Triplet Electron Resonance Spectroscopy, J. Phys. Chem. Lett., 80–85, https://doi.org/10.1021/acs.jpclett.0c02884, 2020.

10 Bertran, A., Barbon, A., Bowen, A. M., and Di Valentin, M.: Chapter Seven - Light-induced pulsed dipolar EPR spectroscopy for distance and orientation analysis, in: Methods in Enzymology, vol. 666, edited by: Britt, R. D., Academic Press, 171–231, https://doi.org/10.1016/bs.mie.2022.02.012, 2022.

Bieber, A., Bücker, D., and Drescher, M.: Light-induced dipolar spectroscopy – A quantitative comparison between LiDEER and LaserIMD, Journal of Magnetic Resonance, 296, 29–35, https://doi.org/10.1016/j.jmr.2018.08.006, 2018.

15 Bücker, D., Sickinger, A., Ruiz Perez, J. D., Oestringer, M., Mecking, S., and Drescher, M.: Direct Observation of Chain Lengths and Conformations in Oligofluorene Distributions from Controlled Polymerization by Double Electron–Electron Resonance, J. Am. Chem. Soc., https://doi.org/10.1021/jacs.9b11404, 2019.

Collauto, A., von Bülow, S., Gophane, D. B., Saha, S., Stelzl, L. S., Hummer, G., Sigurdsson, S. T., and Prisner, T. F.: Compaction of RNA Duplexes in the Cell, Angewandte Chemie International Edition, n/a, 20 https://doi.org/10.1002/anie.202009800, 2020.

Dal Farra, M. G., Richert, S., Martin, C., Larminie, C., Gobbo, M., Bergantino, E., Timmel, C. R., Bowen, A. M., and Di Valentin, M.: Light-induced pulsed EPR dipolar spectroscopy on a paradigmatic Hemeprotein, ChemPhysChem, 0, https://doi.org/10.1002/cphc.201900139, 2019a.

Dal Farra, M. G., Ciuti, S., Gobbo, M., Carbonera, D., and Di Valentin, M.: Triplet-state spin labels for highly sensitive pulsed 25 dipolar spectroscopy, Molecular Physics, 117, 2673–2687, https://doi.org/10.1080/00268976.2018.1503749, 2019b.

Dalaloyan, A., Qi, M., Ruthstein, S., Vega, S., Godt, A., Feintuch, A., and Goldfarb, D.: Gd(iii)-Gd(iii) EPR distance measurements - the range of accessible distances and the impact of zero field splitting, Phys. Chem. Chem. Phys., 17, 18464–18476, https://doi.org/10.1039/C5CP02602D, 2015.

Di Valentin, M., Albertini, M., Zurlo, E., Gobbo, M., and Carbonera, D.: Porphyrin Triplet State as a Potential Spin Label for Nanometer Distance Measurements by PELDOR Spectroscopy, J. Am. Chem. Soc., 136, 6582–6585, https://doi.org/10.1021/ja502615n, 2014.

Di Valentin, M., Albertini, M., Dal Farra, M. G., Zurlo, E., Orian, L., Polimeno, A., Gobbo, M., and Carbonera, D.: Light-Induced Porphyrin-Based Spectroscopic Ruler for Nanometer Distance Measurements, Chem. Eur. J., 22, 17204–17214, https://doi.org/10.1002/chem.201603666, 2016.

Edwards, T. H. and Stoll, S.: Optimal Tikhonov regularization for DEER spectroscopy, Journal of Magnetic Resonance, 288, 58–68, https://doi.org/10.1016/j.jmr.2018.01.021, 2018.

Fábregas Ibáñez, L., Jeschke, G., and Stoll, S.: DeerLab: A comprehensive toolbox for analyzing dipolar EPR spectroscopy data, Magn. Reson. Discuss., 2020, 1–28, https://doi.org/10.5194/mr-2020-13, 2020.

García-Rubio, I.: EPR of site-directed spin-labeled proteins: A powerful tool to study structural flexibility, Archives of Biochemistry and Biophysics, 108323, https://doi.org/10.1016/j.abb.2020.108323, 2020.

Giannoulis, A., Feintuch, A., Barak, Y., Mazal, H., Albeck, S., Unger, T., Yang, F., Su, X.-C., and Goldfarb, D.: Two closed ATP- and ADP-dependent conformations in yeast Hsp90 chaperone detected by Mn(II) EPR spectroscopic techniques, Proc Natl Acad Sci USA, 117, 395, https://doi.org/10.1073/pnas.1916030116, 2020.

Hagston, W. E. and Holmes, B. J.: Matrix methods for spin Hamiltonians of low symmetry, J. Phys. B: Atom. Mol. Phys., 13, 3505–3519, https://doi.org/10.1088/0022-3700/13/18/005, 1980.

Hintze, C., Schutze, F., Drescher, M., and Mecking, S.: Probing of chain conformations in conjugated polymer nanoparticles by electron spin resonance spectroscopy, Phys. Chem. Chem. Phys., 17, 32289–32296, https://doi.org/10.1039/C5CP05749C, 2015.

Hintze, C., Bücker, D., Domingo Köhler, S., Jeschke, G., and Drescher, M.: Laser-Induced Magnetic Dipole Spectroscopy, J. Phys. Chem. Lett., 7, 2204–2209, https://doi.org/10.1021/acs.jpclett.6b00765, 2016.

Hogben, H. J., Krzystyniak, M., Charnock, G. T. P., Hore, P. J., and Kuprov, I.: Spinach – A software library for simulation of spin dynamics in large spin systems, Journal of Magnetic Resonance, 208, 179–194, https://doi.org/10.1016/j.jmr.2010.11.008, 2011.

Hu, P. and Hartmann, S. R.: Theory of spectral diffusion decay using an uncorrelated-sudden-jump model, Phys. Rev. B, 9, 1–13, https://doi.org/10.1103/PhysRevB.9.1, 1974.

Hubbell, W. L., López, C. J., Altenbach, C., and Yang, Z.: Technological advances in site-directed spin labeling of proteins, Current Opinion in Structural Biology, 23, 725–733, https://doi.org/10.1016/j.sbi.2013.06.008, 2013.

Jeschke, G.: DEER Distance Measurements on Proteins, Annu. Rev. Phys. Chem., 63, 419–446, https://doi.org/10.1146/annurev-physchem-032511-143716, 2012.

Jeschke, G.: Dipolar Spectroscopy–Double-Resonance Methods, eMagRes, 5, 1459–1476, 2016.

Jeschke, G., Chechik, V., Ionita, P., Godt, A., Zimmermann, H., Banham, J., Timmel, C. R., Hilger, D., and Jung, H.: DeerAnalysis2006—a comprehensive software package for analyzing pulsed ELDOR data, Applied Magnetic Resonance, 30, 473–498, https://doi.org/10.1007/BF03166213, 2006.

Jeschke, G., Sajid, M., Schulte, M., Ramezanian, N., Volkov, A., Zimmermann, H., and Godt, A.: Flexibility of Shape-Persistent Molecular Building Blocks Composed of p-Phenylene and Ethynylene Units, J. Am. Chem. Soc., 132, 10107–10117, https://doi.org/10.1021/ja102983b, 2010.

Krumkacheva, O. A., Timofeev, I. O., Politanskaya, L. V., Polienko, Y. F., Tretyakov, E. V., Rogozhnikova, O. Yu., Trukhin, D. V., Tormyshev, V. M., Chubarov, A. S., Bagryanskaya, E. G., and Fedin, M. V.: Triplet Fullerenes as Prospective Spin Labels for Nanoscale Distance Measurements by Pulsed Dipolar EPR, Angewandte Chemie, 585, 13271–13275, https://doi.org/10.1002/ange.201904152, 2019.

Manukovsky, N., Feintuch, A., Kuprov, I., and Goldfarb, D.: Time domain simulation of Gd3+–Gd3+ distance measurements by EPR, The Journal of Chemical Physics, 147, 044201, https://doi.org/10.1063/1.4994084, 2017.

Marko, A., Denysenkov, V., Margraf, D., Cekan, P., Schiemann, O., Sigurdsson, S. Th., and Prisner, T. F.: Conformational Flexibility of DNA, J. Am. Chem. Soc., 133, 13375–13379, https://doi.org/10.1021/ja201244u, 2011.

Marko, A., Denysenkov, V., and Prisner, T. F.: Out-of-phase PELDOR, Molecular Physics, 111, 2834–2844, https://doi.org/10.1080/00268976.2013.807369, 2013.

McLauchlan, K. A., Shkrob, I. A., and Yeung, M. T.: Room-temperature observations of spin-polarized triplet anthracene, Chemical Physics Letters, 217, 157–162, https://doi.org/10.1016/0009-2614(93)E1353-I, 1994.

Pannier, M., Veit, S., Godt, A., Jeschke, G., and Spiess, H. W.: Dead-Time Free Measurement of Dipole–Dipole Interactions between Electron Spins, Journal of Magnetic Resonance, 142, 331–340, https://doi.org/10.1006/jmre.1999.1944, 2000.

Richert, S., Tait, C. E., and Timmel, C. R.: Delocalisation of photoexcited triplet states probed by transient EPR and hyperfine spectroscopy, Journal of Magnetic Resonance, 280, 103–116, https://doi.org/10.1016/j.jmr.2017.01.005, 2017.

Ritsch, I., Lehmann, E., Emmanouilidis, L., Yulikov, M., Allain, F., and Jeschke, G.: Phase Separation of Heterogeneous Nuclear Ribonucleoprotein A1 upon Specific RNA-Binding Observed by Magnetic Resonance, Angewandte Chemie International Edition, n/a, https://doi.org/10.1002/anie.202204311, 2022.

Robotta, M., Gerding, H. R., Vogel, A., Hauser, K., Schildknecht, S., Karreman, C., Leist, M., Subramaniam, V., and Drescher, M.: Alpha-Synuclein Binds to the Inner Membrane of Mitochondria in an α-Helical Conformation, ChemBioChem, 15, 2499–2502, https://doi.org/10.1002/cbic.201402281, 2014.

Roser, P., Schmidt, M. J., Drescher, M., and Summerer, D.: Site-directed spin labeling of proteins for distance measurements
5   in vitro and in cells, Org. Biomol. Chem., 14, 5468–5476, https://doi.org/10.1039/C6OB00473C, 2016.

Scherer, A., Yao, X., Qi, M., Wiedmaier, M., Godt, A., and Drescher, M.: Increasing the Modulation Depth of Gd(III)-Based Pulsed Dipolar EPR Spectroscopy (PDS) with Porphyrin-Gd(III) Laser-Induced Magnetic Dipole Spectroscopy, J. Phys. Chem. Lett., accepted, 2022.

Schweiger, A. and Jeschke, G.: Principles of Pulse Electron Paramagnetic Resonance, Oxford University Press on Demand,
10   2001.

Serrer, K., Matt, C., Sokolov, M., Kacprzak, S., Schleicher, E., and Weber, S.: Application of commercially available fluorophores as triplet spin probes in EPR spectroscopy, Molecular Physics, 117, 2688–2699, https://doi.org/10.1080/00268976.2019.1608379, 2019.

Sweger, S. R., Denysenkov, V. P., Maibaum, L., Prisner, T. F., and Stoll, S.: The effect of spin polarization in DEER
15   spectroscopy, Magn. Reson. Discuss., 2022, 1–15, https://doi.org/10.5194/mr-2022-8, 2022.

Tait, C. E. and Stoll, S.: Coherent pump pulses in Double Electron Electron Resonance spectroscopy, Phys. Chem. Chem. Phys., 18, 18470–18485, https://doi.org/10.1039/C6CP03555H, 2016.

Takeda, K., Takegoshi, K., and Terao, T.: Dynamic nuclear polarization by electron spins in the photoexcited triplet state: I. Attainment of proton polarization of 0.7 at 105 K in naphthalene, Journal of the Physical Society of Japan, 73, 2313–2318,
20   2004.

Telser, J.: EPR Interactions–Zero-Field Splittings, eMagRes, 6, 207–234, 2017.

Timofeev, I. O., Politanskaya, L. V., Tretyakov, E. V., Polienko, Y. F., Tormyshev, V. M., Bagryanskaya, E., Krumkacheva, O. A., and Fedin, M. V.: Fullerene-based triplet spin labels: methodology aspects for pulsed dipolar EPR spectroscopy, Phys. Chem. Chem. Phys., 4475–4484, https://doi.org/10.1039/D1CP05545C, 2022.

25   Weickert, S., Wawrzyniuk, M., John, L. H., Rüdiger, S. G. D., and Drescher, M.: The mechanism of Hsp90-induced oligomerizaton of Tau, Sci Adv, 6, eaax6999, https://doi.org/10.1126/sciadv.aax6999, 2020.

Williams, L., Tischlik, S., Scherer, A., Fischer, J. W. A., and Drescher, M.: Site-directed attachment of photoexcitable spin labels for light-induced pulsed dipolar spectroscopy, Chem. Commun., 56, 14669–14672, https://doi.org/10.1039/D0CC03101A, 2020.

Wojciechowski, F., Groß, A., Holder, I. T., Knörr, L., Drescher, M., and Hartig, J. S.: Pulsed EPR spectroscopy distance measurements of DNA internally labelled with Gd3+-DOTA, Chem. Commun., 51, 13850–13853, https://doi.org/10.1039/C5CC04234H, 2015.

Worswick, S. G., Spencer, J. A., Jeschke, G., and Kuprov, I.: Deep neural network processing of DEER data, Sci Adv, 4,
5   https://doi.org/10.1126/sciadv.aat5218, 2018.

Yang, Y., Chen, S.-N., Yang, F., Li, X.-Y., Feintuch, A., Su, X.-C., and Goldfarb, D.: In-cell destabilization of a homodimeric protein complex detected by DEER spectroscopy, Proc Natl Acad Sci USA, 117, 20566–20575, https://doi.org/10.1073/pnas.2005779117, 2020.

Yee, E. F., Diensthuber, R. P., Vaidya, A. T., Borbat, P. P., Engelhard, C., Freed, J. H., Bittl, R., Möglich, A., and Crane, B.
10   R.: Signal transduction in light–oxygen–voltage receptors lacking the adduct-forming cysteine residue, Nature Communications, 6, 10079, https://doi.org/10.1038/ncomms10079, 2015.